Can Porphyritic Chondrules Form in Planetary Embryo Bow Shocks?

by

Alexandra Marie Perez

A Thesis Presented in Partial Fulfillment
of the Requirements for the Degree
Master of Science

Approved March 2018 by the
Graduate Supervisory Committee:

Steven J. Desch, Chair
Christy B. Till
Devin L. Schrader

ARIZONA STATE UNIVERSITY

August 2018

ABSTRACT

An exhaustive parameter study involving 133 dynamic crystallization experiments was conducted, to investigate the validity of the planetary embryo bow shock model by testing whether the cooling rates predicted by this model are consistent with the most dominant chondrule texture, porphyritic. Results show that using coarse-grained precursors and heating durations ≤ 5 minutes at peak temperature, porphyritic textures can be reproduced at cooling rates ≤ 600 K/hr, rates consistent with planetary embryo bow shocks. Porphyritic textures were found to be commonly associated with skeletal growth, which compares favorably to features in natural chondrules from Queen Alexandra Range 97008 analyzed, which show similar skeletal features. It is concluded that the experimentally reproduced porphyritic textures are consistent with those of natural chondrules. This work shows heating duration is a major determinant of chondrule texture and the work further constrains this parameter by measuring the rate of chemical dissolution of relict grains. The results provide a robust, independent constraint that porphyritic chondrules were heated at their peak temperatures for ≤ 10 minutes. This is also consistent with heating by bow shocks. The planetary embryo bow shock model therefore remains a viable chondrule mechanism for the formation of the vast majority of chondrules, and the results presented here therefore strongly suggest that large planetary embryos were present and on eccentric orbits during the first few million years of the Solar System's history.

ACKNOWLEDGMENTS

I gratefully thank all those who have dedicated their time to make the completion of this thesis possible. I especially would like to thank Steven Desch. Without him, I would have not had the opportunity to be a graduate student at the School of Earth and Space Exploration. I am forever indebted to his generosity and support. I also would like to thank Christy Till. She believed in me and I recall her saying "people like you deserve to be here and never give up". Thank you, Christy, I made it this far! I thank Devin Schrader for sharing his expertise on chondrules as well as designing the experimental set up to make this all possible. The entire EPIC team has created an encouraging and supportive atmosphere – no matter how many questions I asked. It was an honor to work with you all. Special thanks to Axel Wittmann for being kind and patient with me while training me to use the EPMA as well as providing great and meaningful conversations on minerals and textures. I also would like to acknowledge his help on writing the operating conditions necessary for the electron microprobe analyses.

I express my sincere gratitude to Dr. Haraldur Karlsson, my senior advisor at Texas Tech University. Without him, this journey would have never even begun. I also am grateful for Dr. Aaron Yoshinobu. He believed I can do anything I set my mind to. A big thank you to all of my professors at both Texas Tech University and Arizona State University who helped me become the aspiring scientist I am today. I also thank my dogs, Rocky and Rambo, for providing all the pet therapy (mostly annoying) to get through the program and my family for their support.

Lastly, I would like to thank: the Smithsonian Institution, the members of the Meteorite Working Group, Cecilia Satterwhite and Kevin Righter (NASA, Johnson Space Center) for the sample of QUE 97008 that was used in this work. US Antarctic meteorite samples are recovered by the Antarctic Search for Meteorites (ANSMET) program, which has been funded by NSF and NASA, and characterized and curated by the Department of Mineral Sciences of the Smithsonian Institution and Astromaterials Curation Office at NASA Johnson Space Center. I am grateful to Sam Dunaway, owner of Morefield Gem Mine in Amelia County, Virginia for providing the albite for this work.

TABLE OF CONTENTS

Page

LIST OF TABLES

LIST OF FIGURES

Figure Page

CHAPTER 1

INTRODUCTION

Meteorites and their Significance

Once meteors survive the passage through Earth's atmosphere, such particles that are large enough and/or are able to withstand thermal processes (i.e. heated to fusion and incandescence by friction) arrive to Earth's surface as meteorites (Dodd, 1981). Meteorites are key to unlocking the secrets to the origins and evolution of the Solar System and provide us with direct samples without having to develop extensive and expensive missions to acquire them, thus earning the nickname "the poor man's space probe". Meteorites are classified into three major categories based on their abundance of silicates as well as their iron-nickel content. Iron meteorites are comprised entirely of iron-nickel. Stony iron meteorites, which are thought to be representative of the core-mantle boundary of a planet, contain nearly equal proportions of silicates and iron-nickel. Common examples in this category include pallasites and mesosiderites. Lastly, stony meteorites consist predominantly of silicates and can be broken down into two groups: chondrites and achondrites. The primary difference between the two is the presence of chondrules, which will be discussed shortly. Chondrites are the most primitive of all the meteorites with a $^{206}Pb/^{204}Pb$ age of 4,566.6 ± 1.0 million years (Amelin and Krot, 2007). Their main constituents include chondrules, calcium aluminum-rich inclusions (CAIs), refractory inclusions, and matrix. However, chondrites are subdivided into 15 different groups on based on their chemical makeup, oxygen isotopic signatures, and mineralogy, and some groups contain more CAIs, for example, than others.

Chondrules and their Textures

Chondrules are sub-mm to mm-sized igneous inclusions that can comprise up to ~80% (Weisberg et al. 2006) of the primitive meteorites called chondrites and are the key to understanding the early history of the Solar System and the formation of terrestrial planets. This is because chondrules formed in the first few million years (Myr) of the Solar System's history during its protoplanetary disk phase (e.g., Kita and Ushikubo, 2012), and originated as free-floating objects in the solar nebula. Thus, understanding the energetic event(s) that melted chondrules is key to using meteoritic data to constrain astrophysical models of the disk.

Chondrules display an array of igneous textures that are the result of melting and recrystallization that occurred as they floated freely in the protoplanetary disk, with the textures reflecting the differences in the appearance (e.g., size, shape, orientation) of phenocrysts (melt-grown crystals) within a fine-grained matrix or mesostasis. The three most common chondrule textures, in the order of their abundance, are: (1) porphyritic, (2) radial, and (3) barred (e.g., Jones, 2012) as shown in Figure 1. Porphyritic textures are typically defined as having subhedral to euhedral grains of olivine and/or pyroxene within a fine-grained matrix or mesostasis. Such textures require the retention of up to hundreds of seed nuclei or previously existing crystals to create the classic porphyritic textures observed. Radial textures grow during rapid growth from glass (no seed nuclei) and consist of thin laths (few microns in thickness) of pyroxene that radiate from one or more points, producing a fan-like or shell-like morphology. Barred olivine chondrules can be viewed as a transitional texture between porphyritic and radial chondrules and consists of olivine laths set in a preferred orientation within a glassy mesostasis. The

retention of some nucleation sites is required to form barred olivine chondrules. Porphyritic textures dominate the chondrule population, accounting for up to ~99% of chondrules in some chondrites (Jones, 2012), therefore any chondrule formation model must be consistent with these textures in particular. Determining the factors that produce these textures thus place constraints on conditions and processes in the solar nebula to constrain chondrule formation mechanisms.

In this thesis we experimentally investigate whether the planetary embryo bow shock mechanism (Morris et al. 2012; Mann et al. 2016) would melt chondrules in a manner that would yield porphyritic textures.

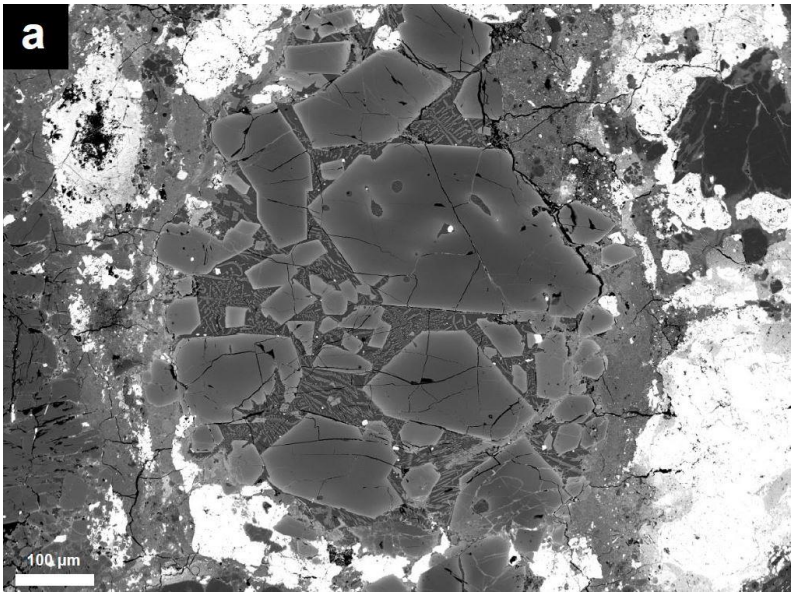
a
100 µm

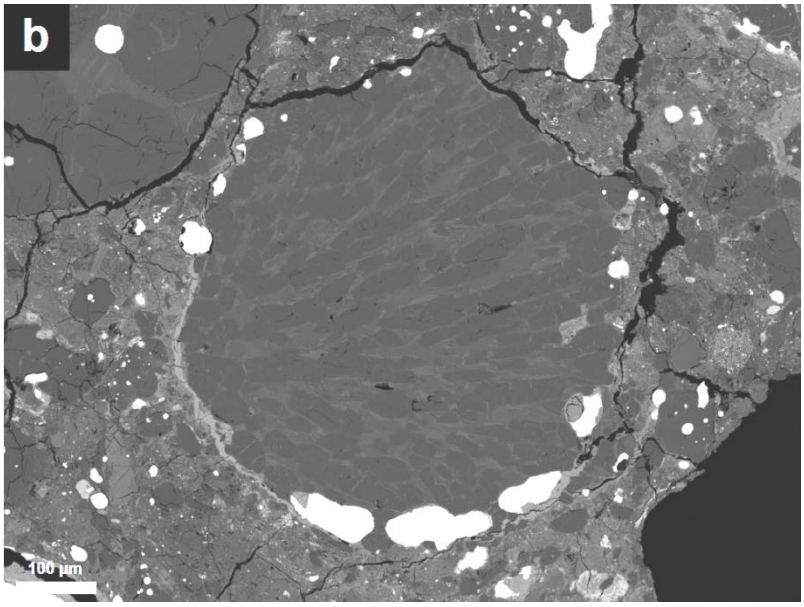
b
100 µm

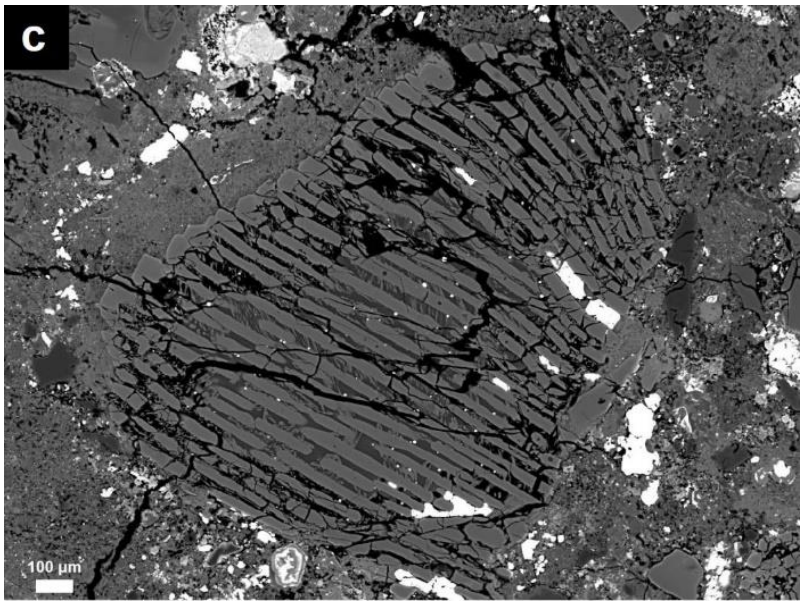

Figure 1. BSE images of natural chondrules. a) Porphyritic chondrule from QUE 97008. b) Radial pyroxene chondrule from Yamato-002540. Image courtesy of Devin Schrader. c) Barred olivine chondrule from QUE 97008. Scale bars are 100 µm.

Constraints for a Successful Chondrule Formation Model

There are both thermal and physical constraints that any proposed chondrule formation model must be able to satisfy (see review by Desch et al. 2012), with thermal constraints being more restrictive. Based on the existence of primary sulfur in chondrule melts, the ambient temperature must not have exceeded 650 K, as S condenses (as troilite) only below this temperature (Anders 1964; Bland et al. 2005; Desch et al. 2012). Chondrule formation models also must be consistent with heating durations on the orders of only a few minutes (< 10 minutes) as constrained by the preservation of volatiles such Na and K in chondrule glasses, as well as the lack of isotopic fractionation of volatiles such as K, S, Fe (Alexander et al. 2008; Desch et al. 2012). An independent and more robust constraint on heating duration comes from dissolution rate calculations, and these

also indicate heating durations on the order of minutes (Soulié et al. 2017). Finally, peak temperatures and cooling rates during crystallization are strongly constrained by chondrule textures and suggest peak temperatures exceeding 1600 K and cooling rates comparable to 1000 K/hr or less.

Another important constraint that a prospective chondrule formation model must meet is its ability to explain the frequency of compound chondrules. This frequency has been calculated to be 4% (Gooding and Keil, 1981). Compound chondrules are two chondrules fused together and there are three types: adhering, consorting, and enveloping (Wasson et al., 1995), all of which involve a primary chondrule and a secondary chondrule that is typically smaller in size than the primary (Figure 2). Their formation mechanism is not certain and arguments suggest they were either formed by molten droplet collisions (e.g., Ciesla et al. 2004) or collisions of supercooled droplets (Arakawa and Nakamoto, 2016). The main difference between compound chondrules and single chondrules is that single chondrules are partially molten, whereas compound chondrules are most likely completely molten (Arakawa and Nakamoto, 2016). Arakawa and Nakamoto (2016) show the cooling rates required to form compound chondrules correlate nicely with the cooling rates presented by Desch et al. (2012), up to 3600 K/hr.

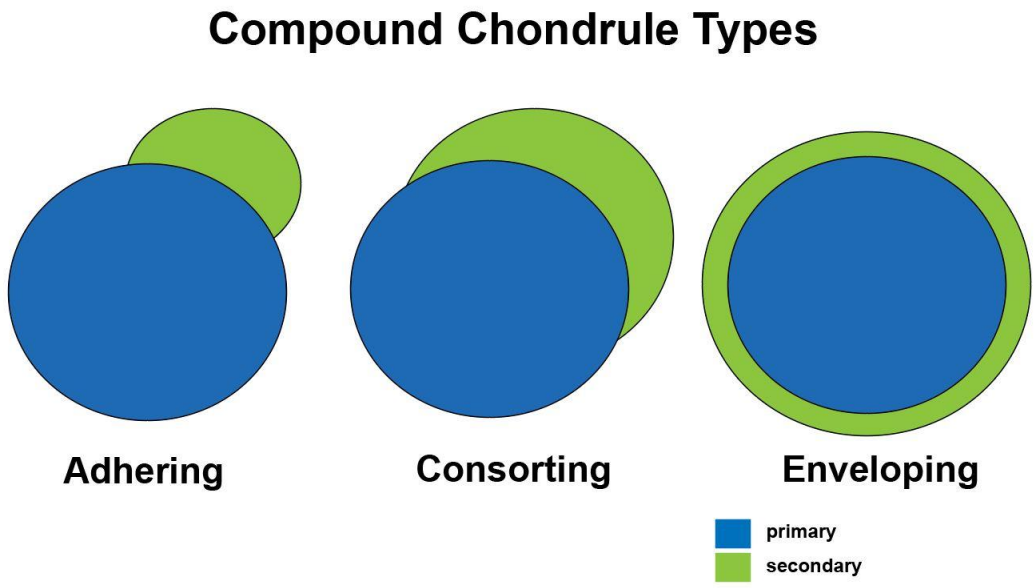

Figure 2. Types of compound chondrules.

Previous Experiments

One of the methods to determine the conditions necessary to reproduce chondrule textures is through dynamic crystallization experiments, by investigating factors that can control chondrule texture. (Lofgren Russell, 1986; Lofgren, 1989; Radomsky and Hewins, 1990). Commonly investigated parameters, which are also investigated in this study, include grain size, peak temperature, heating duration, and cooling rate. Grain size refers to the initial size of the particles comprising the chondrule precursors. Peak temperature is the highest temperature the experimental chondrule analogs are raised to prior to cooling, and heating duration refers to the length of time at which chondrule precursors remained at their peak temperatures. Cooling rate refers to changing in temperature with time between its liquidus and solidus temperatures. Figure 3 illustrates

the cooling rates of prior experiments and the resulting different chondrule textures where Type I chondrules are FeO-poor and Type II chondrules are FeO-rich.

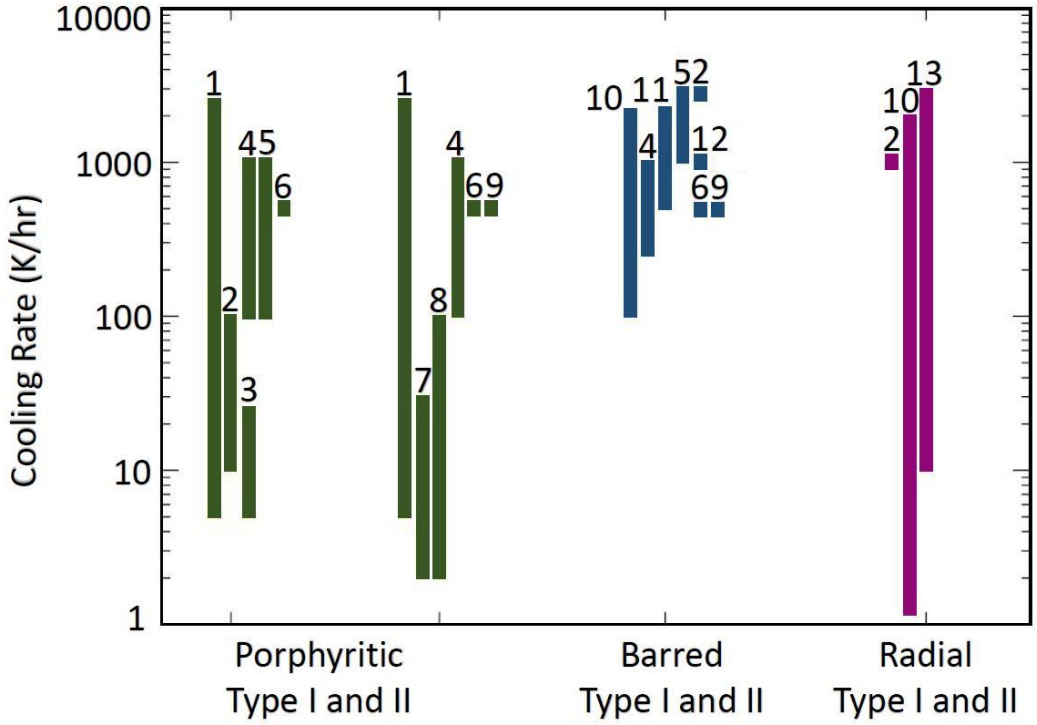

Figure 3. Chondrule textures at various cooling rates from previous experimental studies. 1. Lofgren and Russell (1986); 2. DeHart and Lofgren (1996); 3. Wick and Jones (2012); 4. Radomsky and Hewins (1990); 5. Lofgren (1989); 6. Connolly and Hewins (1991); 7. Weinbruch and Müller (1995); 8. Jones and Lofgren (1993); 9. Connolly et al. (1998); 10. Kennedy et al. (1993); 11. Lofgren and Lanier (1990); 12. Tsuchiyama et al. (2004);13. Hewins et al. (1981). Modified from Desch et al. (2012).

While cooling rates are an important factor determining chondrule texture, other experimental conditions also prove important and have not been investigated systematically. All prior studies investigated the effects of peak temperature, considering a range of peak temperatures above and below the liquidus temperature (calculated from

the starting bulk compositions of the chondrule analogs) as shown in Table 1. Only a few past studies (e.g., Connolly and Hewins, 1991; Connolly et al. 1998; Nettles et al. 2005) have investigated the significance grain size fractions pose on chondrule textures. Because chondrule formation models had not been able to predict this important quantity, previous experiments investigated a very wide range of heating durations. For example, Connolly et al. (1998) used a heating duration of < 1 minute and Lofgren and Russell (1986) used heating durations > 1000 minutes for some of their experiments. The importance of heating duration is returned in the Discussion section. For at least some combinations of these factors, porphyritic chondrules are generally reproduced at cooling rates up to 1000 K/hr with the exception those reproduced at 2500 K/hr by Lofgren and Russell (1986). Barred olivine chondrules are experimentally reproduced at cooling rates up to 3100 K/hr (Lofgren and Russell, 1986), and radial textures expand a wide range of cooling rates upwards to 3000 K/hr (Hewins et al. 1981).

Table 1. Literature review of past experiments. Heating duration is the variable that is being focused on when determining whether or not a certain study has met the thermal constrains previously described. Heating durations greater than 10 - 15 minutes were determined to not have met these constraints that chondrules were heated for < 10 minutes based on the retention of Na and K.

Study	**Heating Duration (mins)**	**Grain Size (μm)**	**Peak Temperature (°C)**	**Texture / Cooling Rate (K/hr)**	**Met Thermal Constraints**
Lofgren and Russell (1986)	180 - 1020	Not specified	A few degrees C above and below liquidus for various starting compositions	Porphyritic (5 - 3100) Barred (5 - 100) Radial	No

				(5 - 3100)	
DeHart and Lofgren (1996)	30	Not specified	L = 1555 L - 15, L - 5, L + 5	Porphyritic (10 - 1000) Barred (100 - 1000)	No
Wick and Jones 2012	18	Not specified	L - 100	Radial (2800) Porphyritic (5 - 25)	No
Radomsky and Hewins (1990)	30 - 240	Not specified	Above, near, and below liquidus	Porphyritic (10 - 1000)	No
Lofgren (1989)	120	Not specified	1550, 1570, 1585, 1600	Barred (100 - 1000) Porphyritic (100)	No
Connolly and Hewins (1991)	30	23 - 100	1556, 1610	Barred (100,1900) Porphyritic (500)	No
Jones and Lofgren (1993)	120 - 180	Not specified	L = 1580 L - 30, L - 55	Barred (500) Porphyritic (2 - 100)	No
Connolly et al. (1998)	0	20 - 249	1225 - 1600	Porphyritic (500)	Yes
Kennedy et al. (1993)	60 - 1440	Not specified	1150 - 1425	Barred (500) Barred (100 - 2191)	No
Lofgren and Lanier (1990)	15 - 120	Not specified	1570 - 1640	Radial (1 - 2000) Barred (500 - 2000)	No
Tsuchiyama et al. (2004)	2 - 120	Not specified	L = 1215 1238 - 1418	Barred (500 - 1000)	Yes
Hewins et al. (1981)	120	Not specified	L = 1445 L + 10	Radial (10 - 3000)	No
Nettles et al. (2005)	60	50 - 500	1250, 1350, 1370, and 1450	Porphyritic (10 - 1000)	No

Models for Chondrule Formation

To date, the community has not settled on an astrophysical model for chondrule formation, making it difficult to use the rich and detailed data from chondrules (i.e. petrology, chemical composition, isotopic fractionation, compound chondrule frequency)

to constrain conditions and processes in the protoplanetary disk. Models in which chondrule precursors pass through shock waves in the solar nebula have emerged as a popular chondrule formation mechanism. These models include large-scale (spiral-density) shocks (Hood and Horanyi, 1991; Wood, 1996; Boss, 2002; Boss and Durisen, 2005), and bow shocks around planetary embryos (Morris et al. 2012; Boley et al. 2013; Mann et al. 2016). These two types of shocks would occur in different astrophysical settings, with large-scale shocks driven by gravitational instabilities perhaps favored earlier in disk evolution, while bow shocks around planetary embryos would not occur until later in disk evolution. The prominent difference in terms of thermal histories is that large-scale shocks suggest lower cooling rates, as low as 10 K/hr, but possibly as fast as 1000 K/hr, depending on chondrule density; while embryo bow shocks are more consistent with faster cooling rates, generally hundreds of K/hr or higher. Other proposed chondrule formation mechanisms include the X-wind Model (Shu et al. 1996, 1997, and 2001), nebular lightning (e.g., Desch and Cuzzi 2000), asteroidal impacts (e.g., Urey and Craig, 1953; Asphaug et al. 2011; Johnson et al. 2015; Lichtenberg et al. 2018), current sheets (e.g., Joung et al. 2004; McNally, 2013), and planetesimal bow shocks (e.g. Hood, 1998; Ciesla et al. 2004a). It is important to note that chondrules present in different types of chondrites can be formed by different formation mechanism(s). For example, CB chondrules are known to have been formed by impact generated melt-gas plumes (e.g., Wasson and Kallemeyn, 1990; Campbell et al., 2002; Krot et al., 2017). The research presented here focuses on the formation mechanism that has formed *most* of the chondrules observed in chondrites.

X-Wind Model

One of the initial proposed models for chondrule formation is that of the x-wind (Shu et al. 1996, 1997, and 2001) where the x-wind region is less than 0.5 AU from a protostar. In this model the point of interaction between the Sun's magnetic field and the disk creates an "X" shape geometry. Chondrules lofted by a magnetocentrifugal wind are heated by direct sunlight and subsequently lifted from the disk, cooling as they traverse to the cooler environment of the asteroid belt region (Figure 4). This model is not consistent with the meteoritic data for chondrules and has been dismissed as a chondrule formation mechanism (Desch et al. 2010). However, this model predicts cooling rates that are orders of magnitude lower than those that would be needed to reproduce barred olivine chondrules (Desch et al. 2010).

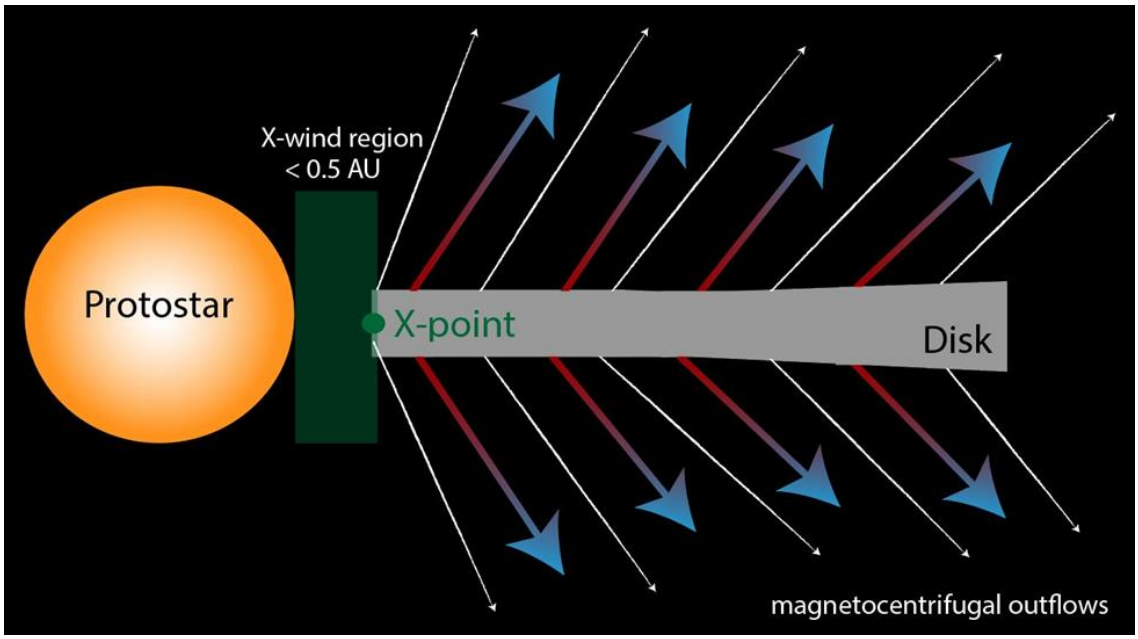

Figure 4. Cartoon of the X-wind model showing the trajectory of chondrules (large arrows) being lofted from the disk into cooler regions between magnetocentrifugal outflows. See text for details.

Nebular Lightning

Nebular lightning might be generated in the solar nebula in a similar way to terrestrial lightning and has been considered as a chondrule formation mechanism (Desch and Cuzzi, 2000). Chondrule precursors presumably would be heated and melted by radiation emitted from the ionized channels, 1 to 10 m in diameter (Figure 5). This model does not appear to be consistent with the compound chondrule frequency, as it would predict a frequency much greater than what is observed (Arakawa & Nakamoto, 2016). More importantly, it would not predict cooling rates as slow as even 1000 K/hr and can be eliminated as the dominant chondrule formation mechanism on that basis (Desch et al. 2012).

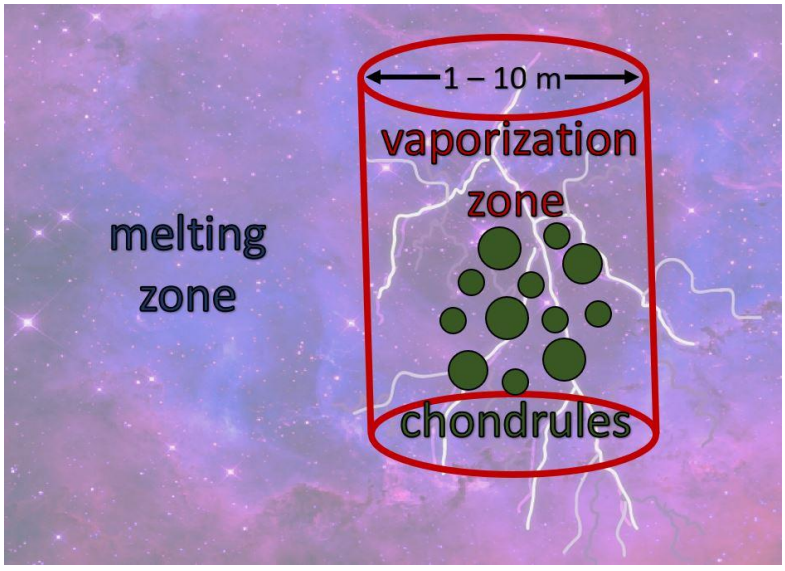

Figure 5. Cartoon of the nebular lightning model in which chondrules are melted within local ionized channels. See text for details.

Large-scale (spiral density) Shocks

Large-scale (> 10^5 km lateral extent), effectively 1-D shocks can be generated by spiral arms launched in the solar nebula either by gravitational instabilities or Jupiter's formation (Hood and Horanyi, 1991; Wood, 1996; Boss, 2002; Boss and Durisen, 2005). In a frame co-moving with the shock, the shock would appear stationary, as depicted in Figure 6. To left of the shock front, there exists a lower-density mix of gas and chondrules approaching the shock front at supersonic velocity ~8 km/s. Once they pass this front, they enter a region of higher density and temperature and subsonic gas velocity, and the chondrule velocities slow by friction over minutes to ~1.3 km/s. During this process, chondrules are being heated by friction, exchange with the hot surrounding gas, as well as the absorption of infrared (IR) radiation emitted by other chondrules. This model predicts cooling rates that are proportional to the chondrule density, ranging from 10 to 1000 K/hr.

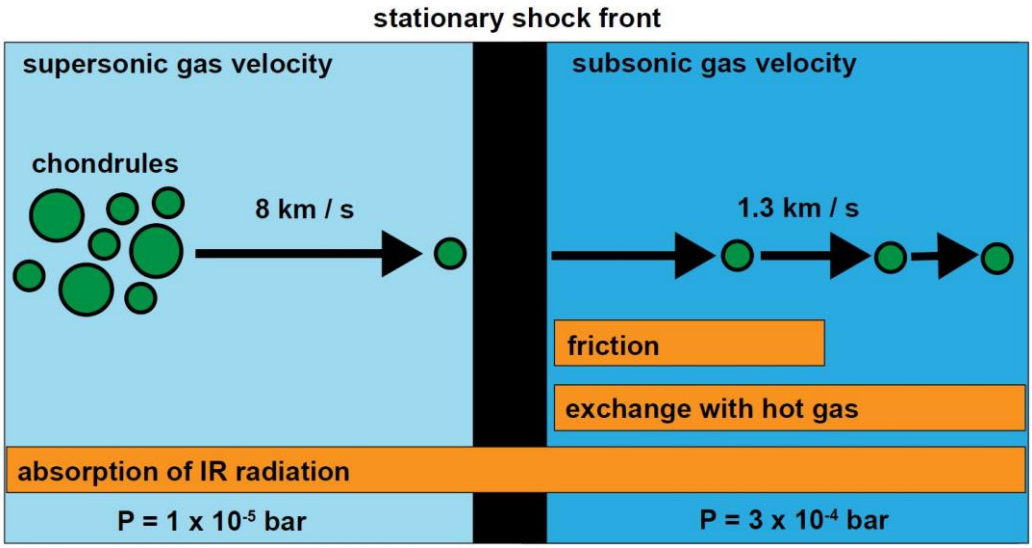

Figure 6. Cartoon of the large-scale (1-D) shock model, drawn in a frame moving with the shock front so that the shock appears stationary. See text for details.

Asteroidal Impacts

A longstanding proposed chondrule formation mechanism is that chondrules are melt droplets formed during the collisions of asteroids (e.g., Urey and Craig, 1953; Asphaug et al. 2011; Johnson et al. 2015; Lichtenberg et al. 2018). A challenge to this model is that collisions are typically not energetic enough to form melt droplets unless the material is already heated within the asteroid; but heating within the asteroid is likely to lead to differentiation, depleting the material of the iron observed in chondrules. Lichtenberg et al. (2018) have shown that a large fraction, but not all, asteroid material may nonetheless satisfy this constraint. The more severe constraint comes from cooling rates. Asphaug et al (2011) investigated cooling rates of melt droplets formed when molten or partly molten planetesimals ~30–100 km diameter, similar in size, collide at velocities comparable to their two-body escape velocity ~100 m/s. They noted that the cooling rate for this mechanism is regulated post collision via the expansion of optically thick sheets and may be ~ 1000 K/hr. Johnson et al. (2015) argued for similar cooling rates. Translating this model into quantitative predictions of cooling rates may require 3-D hydrodynamic simulations with full radiative transfer.

Current Sheets

Similar to lightning, current sheets are another proposed chondrule formation mechanism (e.g., Joung et al. 2004; McNally, 2013). In the inner part of the disk closest to the star exists the warmest part due to thermal ionization. This locality contains turbulent magnetohydrodynamic flows thought to drive accretion in disks. Such flows form thin current sheets hot enough to melt chondrule precursors that pass through them (McNally, 2013). McNally (2013) shows dust grains heated after passage through current

sheets reaching temperatures about 1600 K followed by an increase of temperature after radiating in the near-infrared. However, Desch and Turner (2015) argues that current sheets are not a viable chondrule formation on the basis that short-circuit instability relies on the resistivity of gas decreasing with increasing temperature so that dissipation of magnetic energy during reconnection events can accelerate. Such a condition is met only above ~ 800 K, whereas the ambient temperature where chondrules formed was < 650 K.

Planetesimal Bow Shocks

Planetesimals (~ 100 km in diameter) on eccentric orbits will drive bow shocks in front of them (e.g. Hood, 1998; Ciesla et al. 2004a), velocity differences between the planetesimal and the surrounding gas would drive bow shocks responsible to heat chondrule precursors. Desch et al. (2012) notes that the thermal processing between this mechanism and that of large-scale shocks is nearly identical except radiation can also escape in the lateral direction. Cooling rates would be ~104 K/hr, due to the small size of the planetesimal (Ciesla et al. 2004a). In addition, Morris et al. (2012) note that and chondrules produced in planetesimal bow shocks are likely to remain dynamically decoupled from the surrounding gas and to be subsequently accreted onto the planetesimal. Only in the bow shocks around much larger planetary embryos are the cooling rates potentially low enough to yield the expected textures, and the chondrules given the opportunity to be distributed back into the nebula.

Planetary Embryo Bow Shocks

Planetary embryo bow shocks are formed when the orbital velocity of a planetary embryo (> 1000 km in diameter) differs from that of the surrounding gas by an amount exceeding the sound speed (~ 1 km/s). This generates a shock that serves as a heating

mechanism for chondrules precursors (Figure 7) in a manner similar to other shocks. Because embryos are much larger than planetesimals, the chondrule precursors have time after the shock front to dynamically couple to the gas before they are accreted onto the embryo. Instead, they move away from the embryo and enter much cooler environments off into the solar nebula. This model predicts chondrule cooling rates through the crystallization range as high as 3000 – 5000 K/hr (Morris et al. 2012; Boley et al. 2013), but simulations have shown that dust evaporation can significantly lower these cooling rates to about 2000 K/hr (Mann et al. 2016). Moreover, cooling rates scale roughly inversely with the size of the planetary embryo (Mann et al. 2016), so a larger, Mars-sized embryo should lead to even lower cooling rates, as low as 600 K/hr (Mann et al. 2016). These are potentially consistent with the cooling rates inferred from experiments to date to be consistent with porphyritic textures.

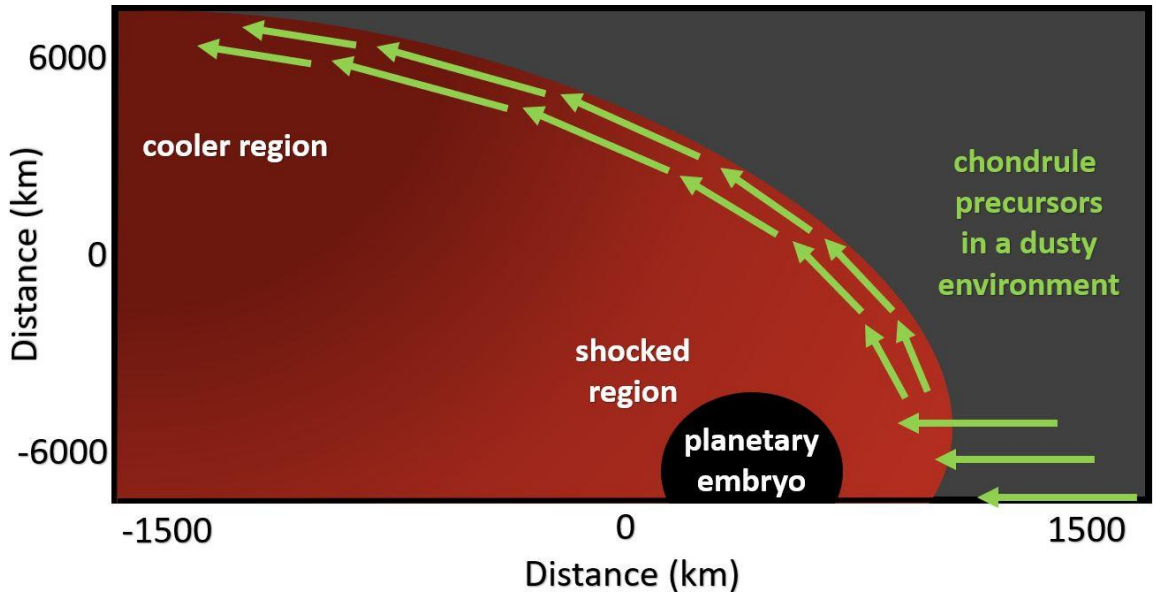

Figure 7. Cartoon of the planetary embryo bow shock model, drawn in a frame moving with the embryo so it appears stationary. Chondrule precursors enter and get heated to

temperatures up to 2500 K in the shocked region (colored red), then couple to the gas and traverse around the embryo into cooler regions. Modified figure from Mann et al. (2016).

Purpose of Study

Melting of chondrules by passage through bow shocks around planetary embryos (several 1000 km in radius) on eccentric orbits offers an excellent match to multiple chondrule properties (Desch et al. 2012). Chondrule formation by planetary bow shocks would take place several Myr into solar system evolution, as large embryos would have to first grow, and Jupiter would have to grow large enough to scatter them onto eccentric orbits; this is consistent with the ages of chondrules derived from Al-Mg, U-Pb, and Hf-W geochronology, which show a range of chondrule formation ages between ~1 and 3.7 Myr (Kita et al., 2000; Villeneuve et al. 2009; Schrader et al., 2017; Budde et al., 2018). Morris et al. (2012) pointed out that chondrules may sample the atmospheres of such planetary embryos, potentially providing the only explanation for the very high inferred partial pressures of Na some chondrules experienced (Alexander et al. 2008). Melting by planetary embryo bow shocks is also consistent with almost all known constraints on chondrules' thermal histories (Desch et al. 2012). Its acceptance as a model has been hindered only by the fact that it generally predicts fast cooling rates, 3000 – 5000 K/hr (Boley et al. 2013), but possibly as low as 1000 K/hr or lower (Mann et al. 2016); whereas porphyritic textures appear to require cooling rates no faster than 1000 K/hr. It is therefore not easy to decide whether bow shocks are consistent with the dominant, porphyritic texture.

Past experiments are not conclusive, because they did not systematically explore cooling rates above 1000 K/hr. The majority of past experiments also did not use appropriate values for other parameters such as heating duration, which are now better constrained by modeling and improved constraints from chondrules. The goal of this thesis work is to investigate the validity of the planetary embryo bow shock model as a chondrule formation mechanism by conducting a series of dynamic crystallization experiments as part of an exhaustive parameter study to see if the cooling rates predicted by this model are consistent with the most dominant chondrule texture, porphyritic.

Here, we present the results of over 100 experiments exploring a range of parameter combinations and compare the experimentally-reproduced porphyritic textures with meteoritic chondrule textures. The experiments are also used to calculate dissolution rates to constrain maximum heating durations for various natural chondrule texture types. Finally, this work demonstrates that the planetary embryo bow shock model is still a viable mechanism to form *most* chondrules.

CHAPTER 2

METHODS

Overview of Approach

To experimentally investigate the planetary embryo bow shock model, natural chondrule analogs with bulk compositions similar to FeO-poor chondrules were created and suspended from a thermocouple inside a 1-atmosphere vertical gas-mixing furnace. The sample underwent various parameter combinations as part of an exhaustive parameter study and the resultant blebs were then prepared for electron probe microanalysis to observe the experimental textures produced. A total of 133 experimental runs were completed.

Description of Furnace

The experiments were carried out inside a 1-atmosphere vertical Deltech gas-mixing furnace located at the School of Earth and Space Exploration's Experimental Petrology and Igneous processes Center (EPIC) at Arizona State University led by principle investigator, Christy B. Till (Figure 8). The furnace used has a maximum working temperature of 1700 K, but due to the 30 K difference present in the thermocouple tubes, the upper limit is 1670 K so this was taken into consideration for the starting bulk composition. The thermocouple used was a Type B (PtRh30/PtRh6). In order to achieve the necessary temperature, the vertical furnace used six molybdenum disilicide (MoSi2) heating elements. The sample was suspended 32.5 cm from a thermocouple inside a mullite tube of type MV-30 material, the hottest point in the

furnace. Desired temperature settings were adjusted using a Eurotherm programmable controller.

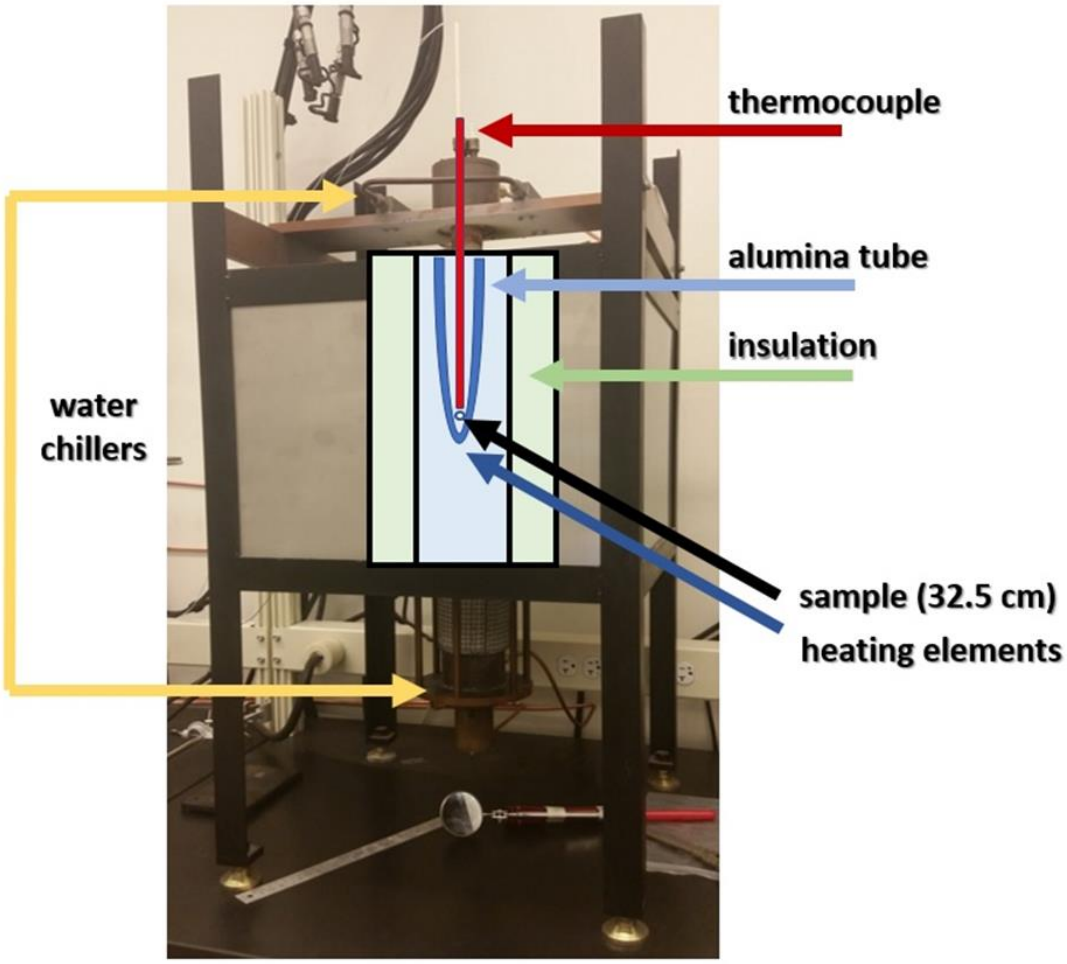

Figure 8. Overview of the vertical furnace and its components.

Calibration Techniques

The oxygen sensor, which is referred to as a calibration probe, is a tool to measure the true temperature of the furnace for the experiments. The specific probe used is a DS-322.7 Type R thermocouple where DS is the model number of the probe and 322.7 is the length of the sensor in millimeters. The probe was also used to determine and

calculate the desired cooling rates. Prior to each experimental run, the calibration probe was used to obtain the temperature of the furnace before suspending the sample to verify the correct peak temperature was obtained as well as obtained the errors for the peak temperatures. The probe connects to a voltmeter where the mV readings are located in *The Temperature Handbook*, 21st century, second edition, volume MM, Handbook and Encyclopedia Temperature, to acquire the temperature.

Starting Composition

Natural chondrule analogs with bulk compositions similar to FeO-poor chondrules were created using a mixture of San Carlos Olivine, Amelia Albite, and Dog Lake Diopside in proportions of 60%, 25%, and 15%, respectively (Hewins and Fox, 2004). This particular bulk composition was also chosen based on the peak temperature constraints of the vertical furnace used. The olivine used in this research originated from the San Carlos xenoliths in San Carlos, Arizona and was provided by Dr. Christy B. Till, Arizona State University. The Amelia Albite was donated by Sam Dunaway, owner of Morefield Gem Mine in Amelia County, Virginia. The Dog Lake Diopside was purchased through Excalibar Mineral Corporation in Houston, Texas. The source used to purchase the diopside was recommended by the Smithsonian Institution's Department of Mineral Sciences. The minerals were initially crushed and separated using the Nikon SMZ18 Stereomicroscope and fine point tweezers. The starting materials minerals were mounted in epoxy and polished using standard polishing procedures, and subsequently carbon coated for wavelength-dispersive spectrometry (WDS) using the JXA-8530F Electron Probe Microanalyzer (EPMA) located in the John M. Cowley Center for High

Resolution Electron Microscopy at Arizona State University with well-characterized natural minerals used as calibration standards. The operating conditions for the analyses were as follows: a beam current of 20 nA and accelerating voltage of 20 kV was used in the analysis. The beam diameter ranged from 1 - 20 µm. A 1-µm beam was used for the analysis of olivine and pyroxene, while the 10 - µm and 20 - µm beam diameters were used for the analysis of plagioclase and glass to avoid beam damage in plagioclase and glass. Counting times for the WDS analyses were 15 seconds on the backgrounds and 30 seconds on the peaks for all elements analyzed. Results of these analyses are shown in Table 2.

Table 2. EPMA analysis of precursor material and bulk composition of the chondrule analogs used. Precision is 1% for major elements.

Oxide	San Carlos Olivine (wt %)	Amelia Albite (wt %)	Dog Lake Diopside (wt %)	Analog (wt %)
SiO_2	40.9	68.6	55.5	49.9
TiO_2	n.a.	n.a.	b.d.l.	b.d.l.
Al_2O_3	n.a.	20.09	0.03	5.03
FeO	9.07	n.a.	0.75	5.55
Cr_2O_3	b.d.l.	n.a.	n.a.	b.d.l.
MnO	0.12	n.a.	0.07	b.d.l.
MgO	50.2	n.a.	18.50	32.9
CaO	0.07	0.46	26.1	4.06
Na_2O	n.a.	11.69	0.06	2.93
K_2O	b.d.l.	0.12	n.a.	0.04
TOTAL	*100.36*	*100.96*	*101.01*	*100.41*

Liquidus: 1608 °C (Herzberg, 1979)

n.a. = not analyzed

b.d.l. = below detection limit

Standards used for analyses (with detection limits) were orthoclase for K_2O (0.01 wt%), orthoclase or Amelia Albite for Al_2O_3 (0.02 wt%), Amelia Albite for Na_2O (0.02 wt%),

rutile for TiO_2 (0.02 wt%), rhodonite for MnO (0.03 wt%), wollastonite for CaO (0.01 wt%), wollastonite, San Carlos Olivine, orthoclase, or Johnstown Hypersthene for SiO_2 (0.02 wt%), San Carlos Olivine or Johnstown Hypersthene for MgO (0.01 wt%), chromite for Cr_2O_3 (0.02), and FeO or Johnstown Hypersthene for FeO (0.03 wt%).

Liquidus, Pressure, and Oxygen Fugacity

The liquidus for the natural chondrule analogs were calculated to be 1608 K using equation A5 from Herzberg (1979) (equation 1) and a forsterite composition of Fo_{90}. The pressure for the experiments is ambient. Due to the restrictions of the furnace in acquiring the higher cooling rates investigated, oxygen fugacity was not used.

$$\ln K = \left[\frac{\left(0.5 n_{Mg^{2+}}\right)_L^2}{\left[\frac{Mg}{Mg + Fe^2 + Ca + Mn}\right]_{ol}^2}\right] + \ln\left(a_{SiO_4^4}\right)_L \left(\gamma_{Mg^{2+}}\right)_L^2 \qquad \text{(eqn. 1)}$$

Grain Size

To systematically investigate the role of grain size and seed nuclei, two different grain size fractions were used (Table 3). One chondrule analog consisted of all fine-grained starting material (63 - 90 μm), and the other analog consisted of fine-grained starting material (63 - 90 μm) of albite and diopside and a larger grain size fraction of olivine (212 - 250 μm). These were selected based on grain size fractions previously investigated by Connolly et al. (1998) ranging from 20 - 249 μm with predominantly microporphyritic textures reproduced using grain size fractions < 63 μm with the parameters investigated.

Table 3. Description of grain sizes for the two different chondrule analogs of similar starting compositions.

Mineral	Analog 1	Analog 2
olivine	63 – 90 µm	212 – 250 µm
albite	63 – 90 µm	63 – 90 µm
diopside	63 – 90 µm	63 – 90 µm

Peak Temperature

Three different peak temperatures were investigated in this study. These included the liquidus, 50 K below the liquidus, and 50 K above the liquidus. The maximum peak temperature of the vertical furnace is 1670 K so this was taken into consideration when we chose the highest peak temperature investigated. The errors associated with the peak temperatures are ± 2 K.

Heating Duration

Heating durations of 1 minute, 5 minutes, and 10 minutes were investigated in this study. As previously discussed, chondrule thermal constraints suggest that heating durations were relatively short (< 10 minutes). Chemical dissolution analyses likewise suggest that natural chondrules were at peak temperatures for no more than 10 minutes (Soulie et al. 2017; see also Chapter 4).

Cooling Rates

A wide range of cooling rates consistent with the planetary embryo bow shock model were investigated which included: 300, 600, 1000, 3000, and 5000 K/hr (Table 4). These cooling rates were achieved by manually lowering the furnace's Eurotherm

controller at rates of 4, 9, 17, 95 K/min, respectively. The 5000 K/hr cooling rate was achieved by removing the thermocouple 1 inch/min. Because of experimental limitations, the actual cooling rates achieved were 300 ± 21, 600 ± 8, 1000 ± 77, 3000 ± 276, and 5000 ± 357 K/hr.

Table 4. Overview of cooling rates investigated.

Cooling Rate (K/hr)	**Method**
300 ± 21	drop 4 K/min
600 ± 8	drop 9 K/min
1000 ± 77	drop 17 K/min
3000 ± 276	drop 95 K/min
5000 ± 357	remove 1”/min

Sample Preparation

Minerals were weighed into the necessary proportions previously described. One-part Elvanol (grade 75 - 15) was added for one part of the mixture to serve as a binding agent. The mixture was then pressed into ~60 mg pellets with a diameter of 3.8 mm. Briefly, an aluminum mold was used in which 50% of the sample was placed and then compressed by hand using a drill rod. One drop of reverse osmosis water was added and the mixture was compressed again. The remaining 50% of the mixture was added and compressed followed by the addition of two drops of reverse osmosis water. The mixture was compressed once more. This process did not affect the initial grain sizes. While still in the mold, the mixture was placed in a Quincy Lab, Inc 20GC Gravity Correction Oven

at 110°C for 45 minutes. The pellets were then allowed to air cool for 15 minutes and subsequently placed inside labeled glass vials prior to being placed in the platinum baskets for experimental runs. The mold allowed for the production of five natural analogs at a time. Analogs were made in advance and were not stored more than 7 days prior to being used for experimental runs.

The platinum wire used was model SPPL-005 purchased from Omega Engineering. This is a fine wire with a 0.005-inch diameter. Platinum baskets were constructed using two wire pieces. The 4-mm diameter basket design is based on durability using four anchor points and two hooks for easy suspension from the thermocouple.

Experimental Technique

For an experimental run, the analog was carefully placed inside the Pt basket. The basket was then suspended from a C-hook at the bottom of the Type B (PtRh30/PtRh6) thermocouple. The thermocouple is then removed from the stand and slowly placed inside the alumina tube. There, the sample underwent multiple parameter combinations (i.e. heating duration, cooling rate). To remove the sample, the thermocouple was slowly lifted from the alumina tube and placed back in the designated stand.

Analysis of Textures

Following the melting and recrystallization of chondrule analogs and after quenching in water for 3 seconds (e.g., Hewins and Fox, 2003), the resultant blebs were placed in epoxy mounts, which were observed using a Nikon Eclipse LV100ND

polarizing/dispersion microscope and then carbon-coated for electron microprobe analysis. Back-scattered electron (BSE) images of the samples were acquired along with semi-quantitative, standardless energy-dispersive spectrometry (EDS) analysis using the EPMA at ASU. A beam current of 20 nA and accelerating voltage of 15 kV was used for these analyses. Chondrule textures were determined by the morphologies of the olivine phenocrysts within the glassy matrix.

CHAPTER 3

RESULTS

Olivine Morphologies

The results of this work show that under several conditions, olivine can evolve into various morphologies observed and described previously by Donaldson (1976). The bulk of the results presented are based on qualitative analyses, so a background in olivine morphology is appropriate. Although no naming convention exists to describe the textures associated with chondrule analogs, the goal of this section is to provide the context necessary to understand the olivine textures by providing higher resolution imagery of the descriptions that will be utilized in this section. Any overview of these textures is shown in Figure 9.

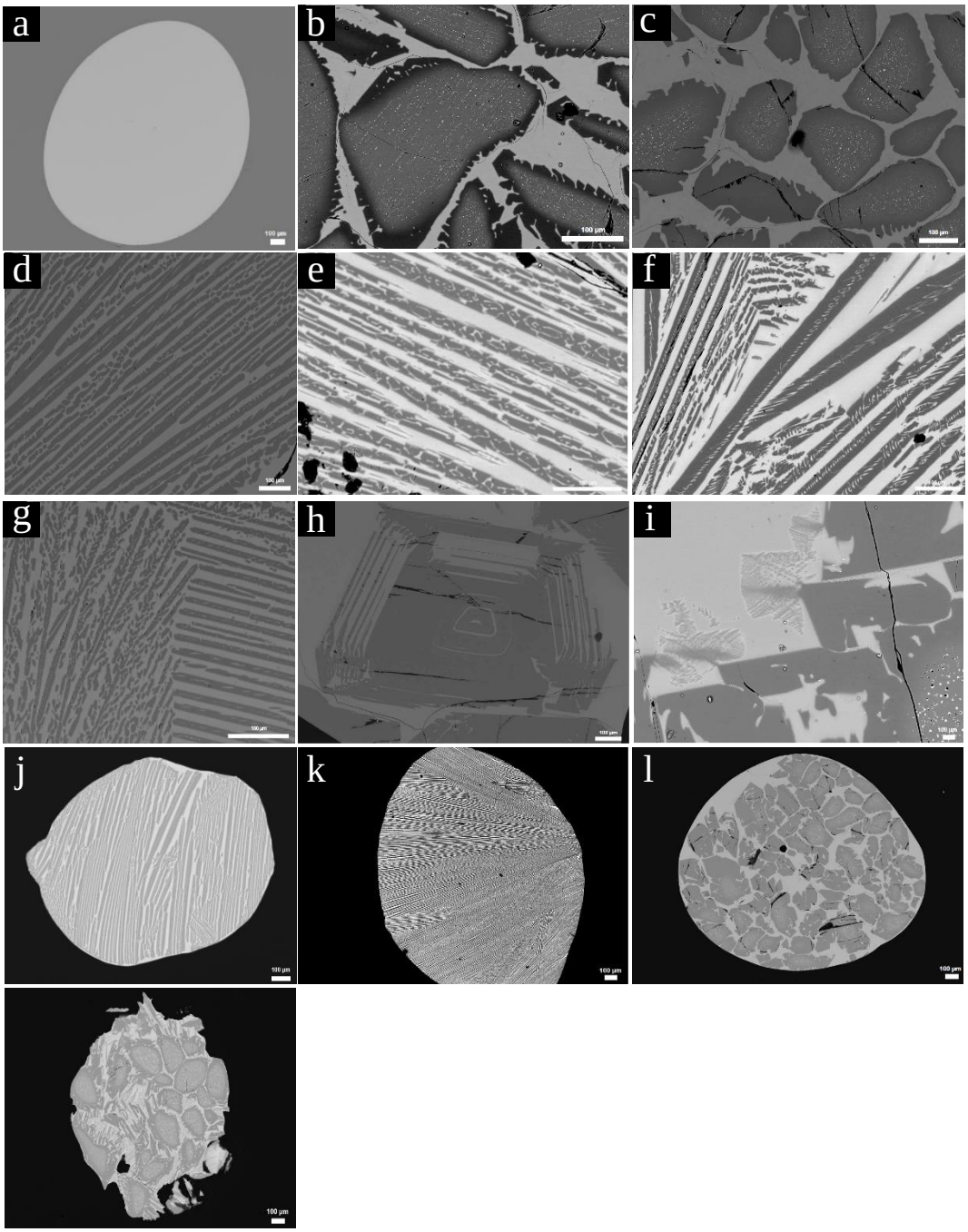

Figure 9. Overview of the different olivine morphologies observed in the experimental results shown in BSE images. See text for descriptions. a) glass. b) relict cores. c) skeletal rim growth. d) plate morphology. e) spinifex texture f) chain morphology g) dendritic

texture h) hopper morphology i) feather texture j) barred texture k) radial texture l) porphyritic texture m) transitional texture. Scale bars are 100 µm.

Glassy textures - show no observed textures within the analog and have no crystals present (Figure 10).

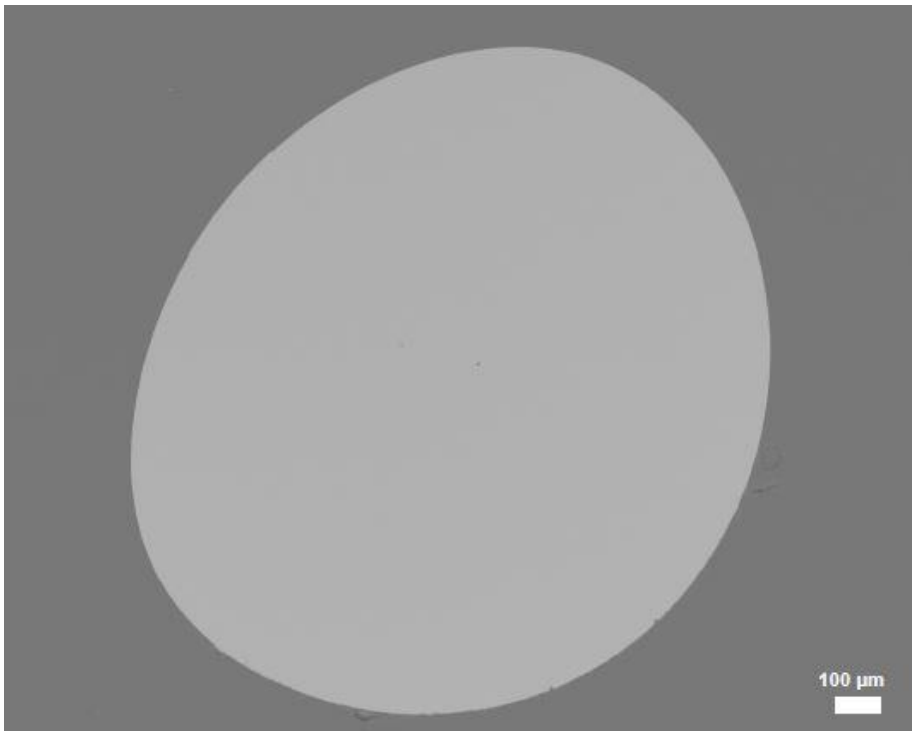

Figure 10. Run 202. BSE image of glass texture produced from an all fine-grained sample heated for one minute at the liquidus and cooled at 600 K/hr. Scale bar is 100 µm.

Anhedral, Euhedral, and Subhedral Grain Shapes- Grain shapes were described using standard igneous petrology terminology. Anhedral grains lack any kind of crystal morphology and sharp edges. Euhedral grains show well-formed crystal faces. These grains are defined by easily recognized, clean edges on the crystals observed in BSE

images. Lastly, subhedral grains show a mixture of the two. These grains have somewhat well-formed crystal faces.

Relict Cores- Grains that did not fully melt during an experimental run and are remnants from the precursor material. They are identified by their high Fe contents, seen as predominantly white spherical inclusions in BSE images (Figure 11). Relict cores look strikingly similar to dusty olivine grains found in chondrules due to the preferred orientations of these inclusions where dusty olivine grains are relatively FeO-poor relict grains containing numerous sub-micron sized grains of pure Fe-metal, which formed by solid-state reduction of relatively more FeO-rich olivine during chondrule formation (e.g., Connolly et al., 1994; Leroux et al., 2003).

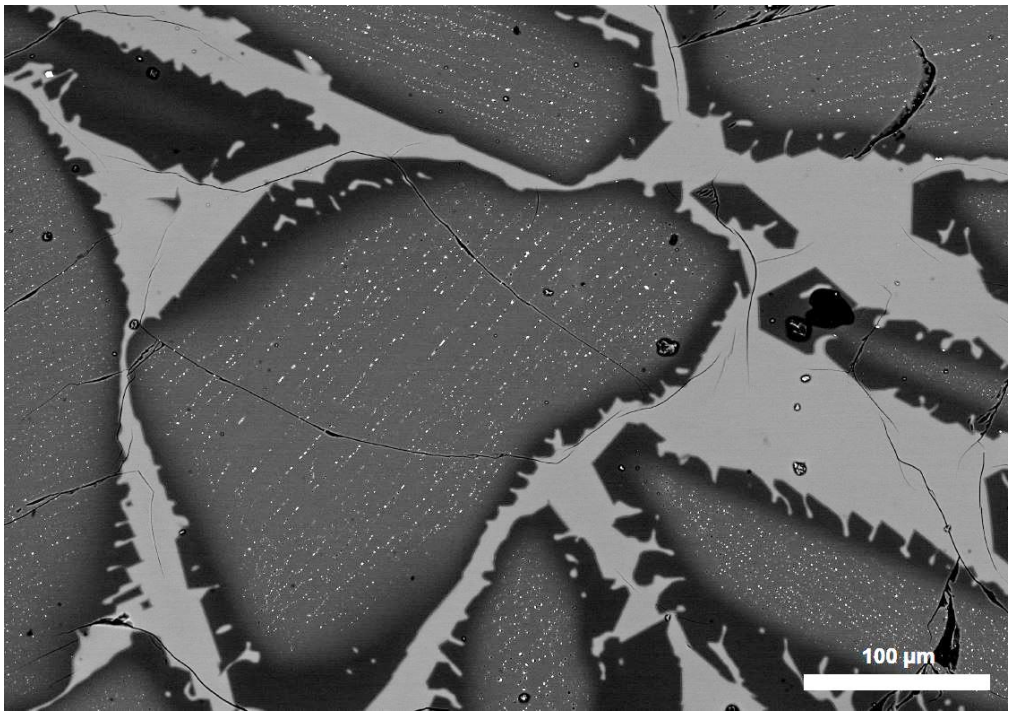

Figure 11. Run 151. BSE image of relict cores from an all fine-grained sample heated for one minute 50 K below the liquidus and cooled at 3000 K/hr. Relict cores are shown with

oriented metal blebs. Skeletal rim growth is shown around the outer regions of the olivine grains. Scale bar is 100 µm.

Skeletal Rim Growth- Skeletal rim growth is observed primarily around relict cores (Figure 12). The thicknesses of these rim growths are only tens of microns. A large portion of the porphyritic-like textures observed show skeletal rim growth around the olivine grains.

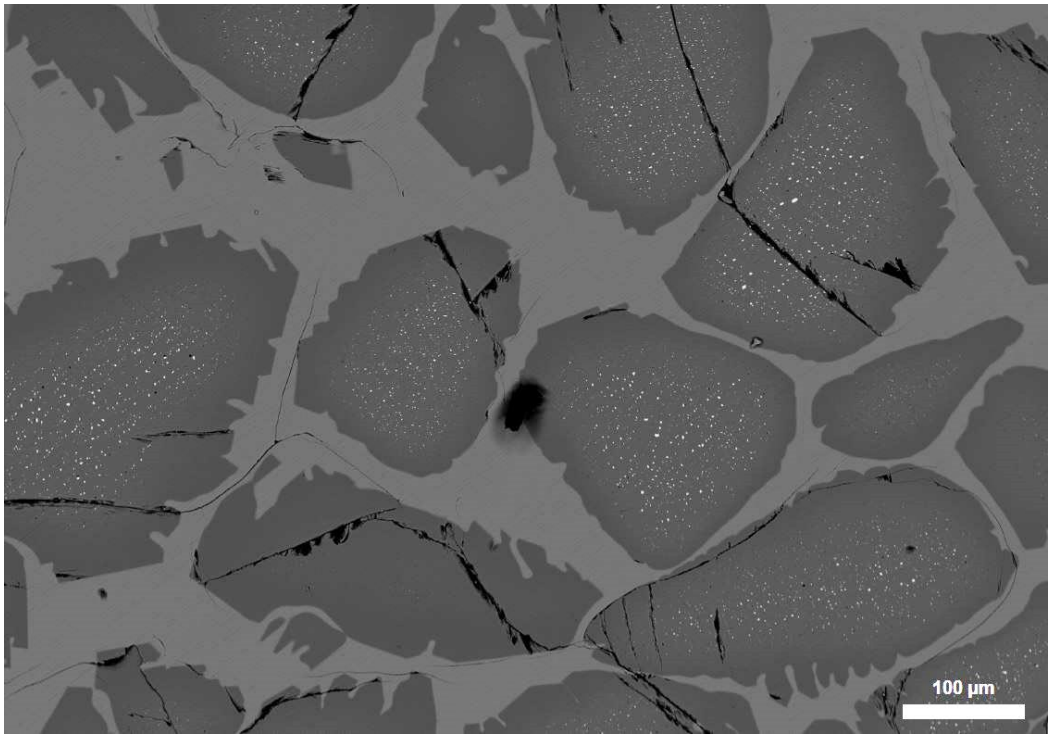

Figure 12. Run 214. BSE image of skeletal rim growth from a fine and large-grained sample heated for one minute 50 K below the liquidus and cooled at 300 K/hr. Skeletal rim growth is present around the perimeter of the olivine grains. Central regions with metal blebs indicate relict cores. Scale bar is 100 µm.

Plate- Plate morphology is a term from Donaldson (1976) where there are two or more parallel tabular grains together (Figure 13). These grains are usually lined up in a preferred orientation.

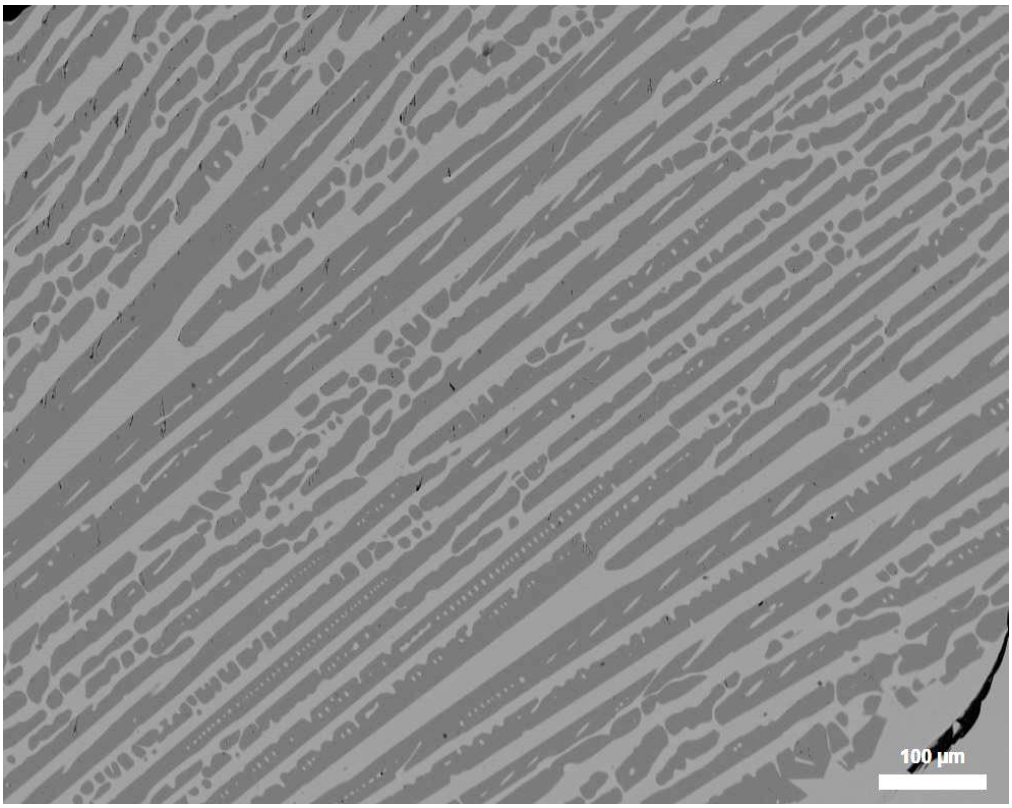

Figure 13. Sample 216. BSE image of plate morphology from a fine and large-grained sample heated for ten minutes 50 K above the liquidus and cooled at 3000 K/hr. Scale bar is 100 µm.

Spinifex- Spinifex textures are characteristic of komatiites, a type of ultra-mafic volcanic rock. The acicular textures are named after a type of Australian grass and can be identified as shaped like blades of grass (Figure 14). This is a quench crystal texture.

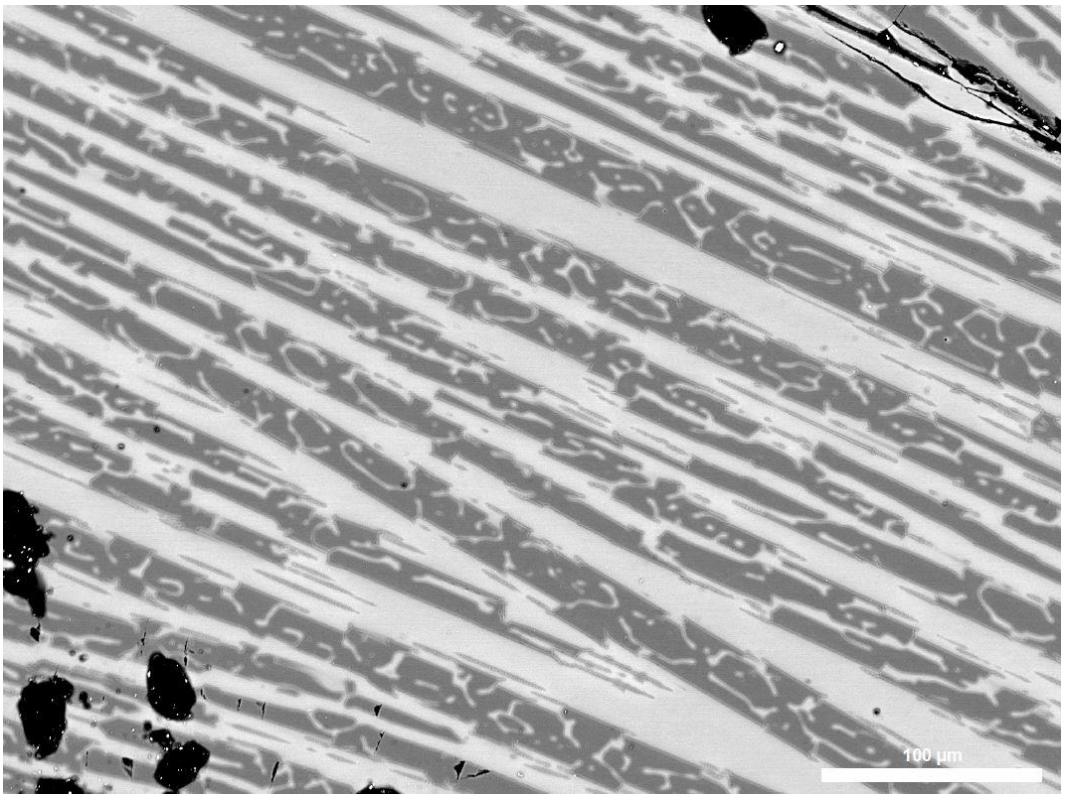

Figure 14. Run 119. BSE image of spinifex texture from a fine and large-grained sample heated for ten minutes 50 K below the liquidus and cooled at 5000 K/hr. Scale bar is 100 µm.

Chain- Chain morphology is another term from Donaldson (1976). Here the crystals are in linked in elongate units to create “chains” (Figure 15).

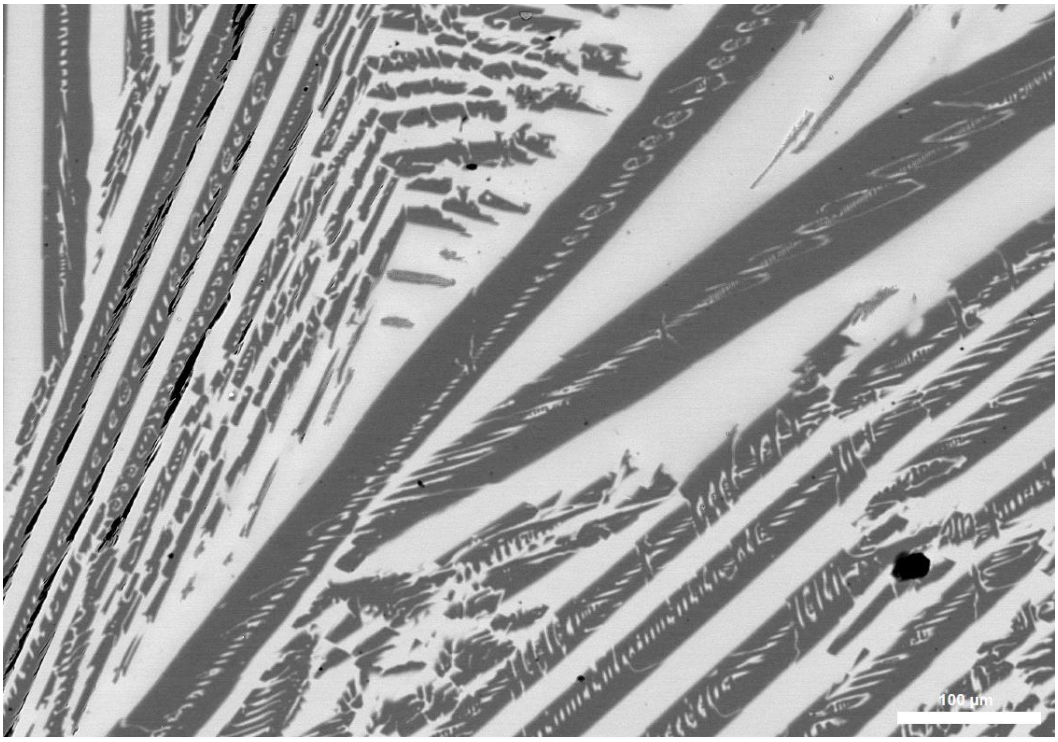

Figure 15. Run 161. BSE image of chain morphology from an all fine-grained sample heated for one minute 50 K above the liquidus and cooled at 5000 K/hr. Scale bar is 100 µm.

Dendritic- Dendritic textures are present when crystals develop multiple branches in a tree-like form (Figure 16).

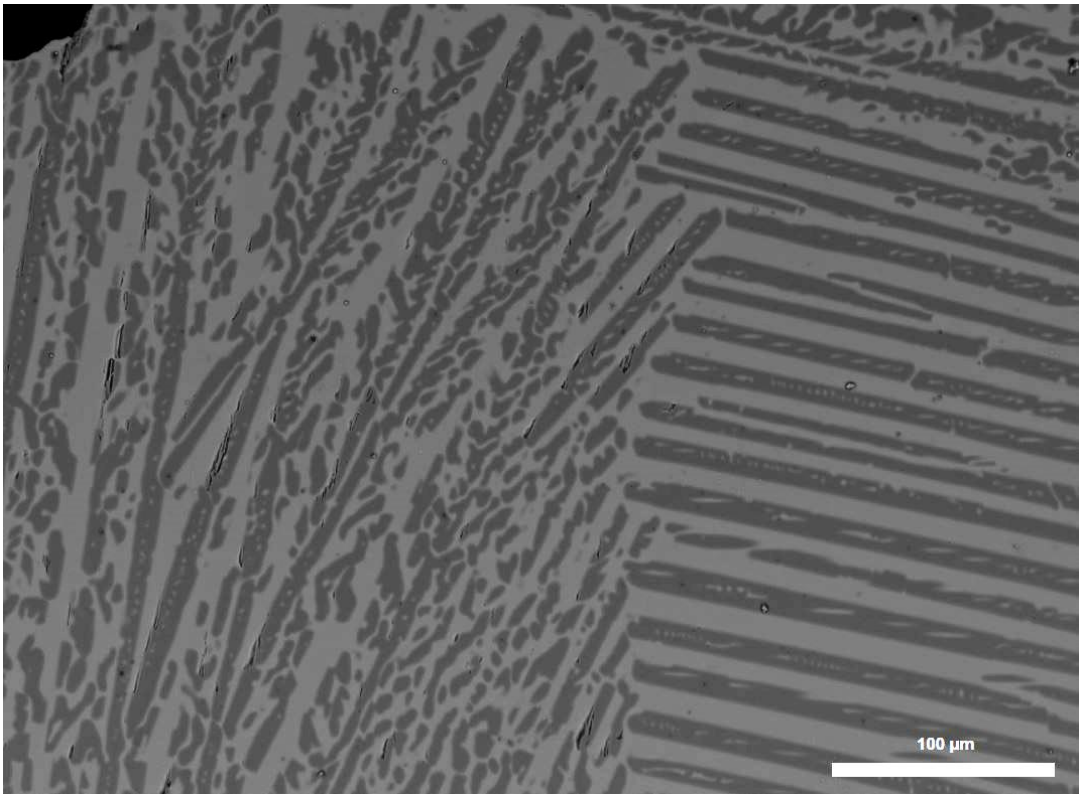

Figure 16. Run 220. BSE image of dendritic texture from an all fine-grained sample heated for five minutes 50 K above the liquidus and cooled at 300 K/hr. Scale bar is 100 µm.

Hopper- Hopper morphology show sub-equant skeletons which retain, with varying degrees of perfection, the gross outline of the common dome and prismatic forms of olivine (Donaldson, 1976) shown in Figure 17. This particular morphology is very common in the experimental runs.

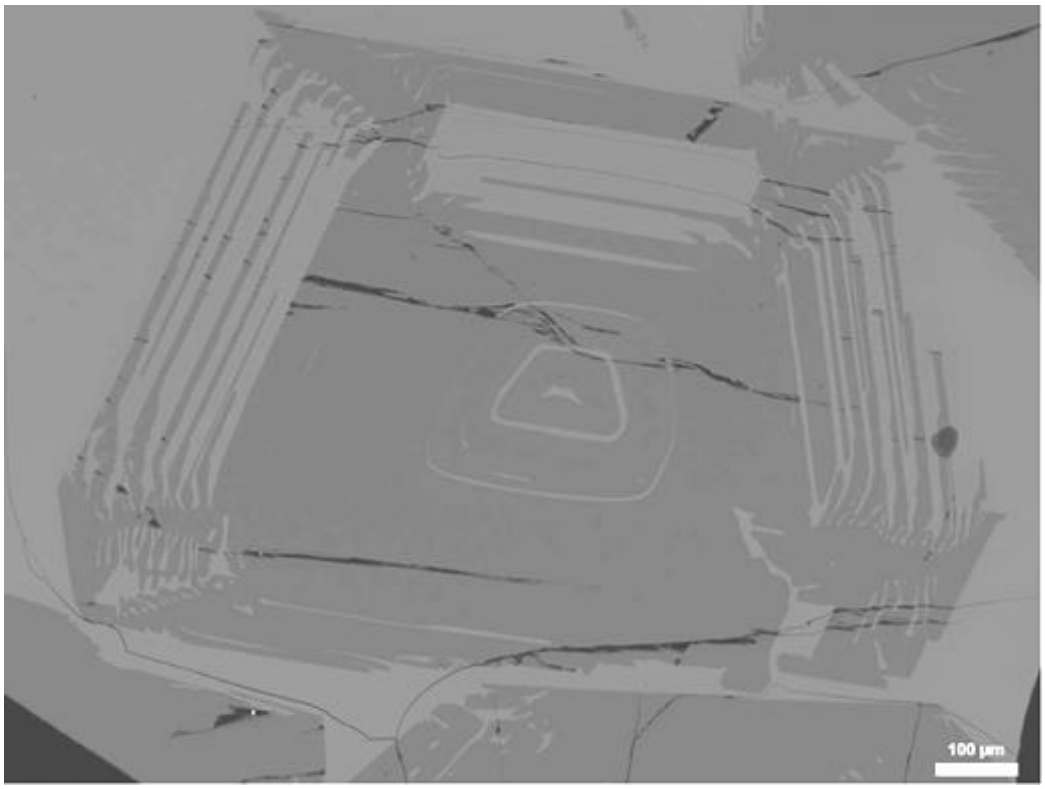

Figure 17. Run 212. BSE image of hopper morphology from an all fine-grained sample heated for ten minutes 50 K below the liquidus and cooled at 300 K/hr. Scale bar is 100 µm.

Feather- Feather texture can be described as that similar to the texture to the veins of a leaf or feather (Donaldson, 1976) shown in Figure 18.

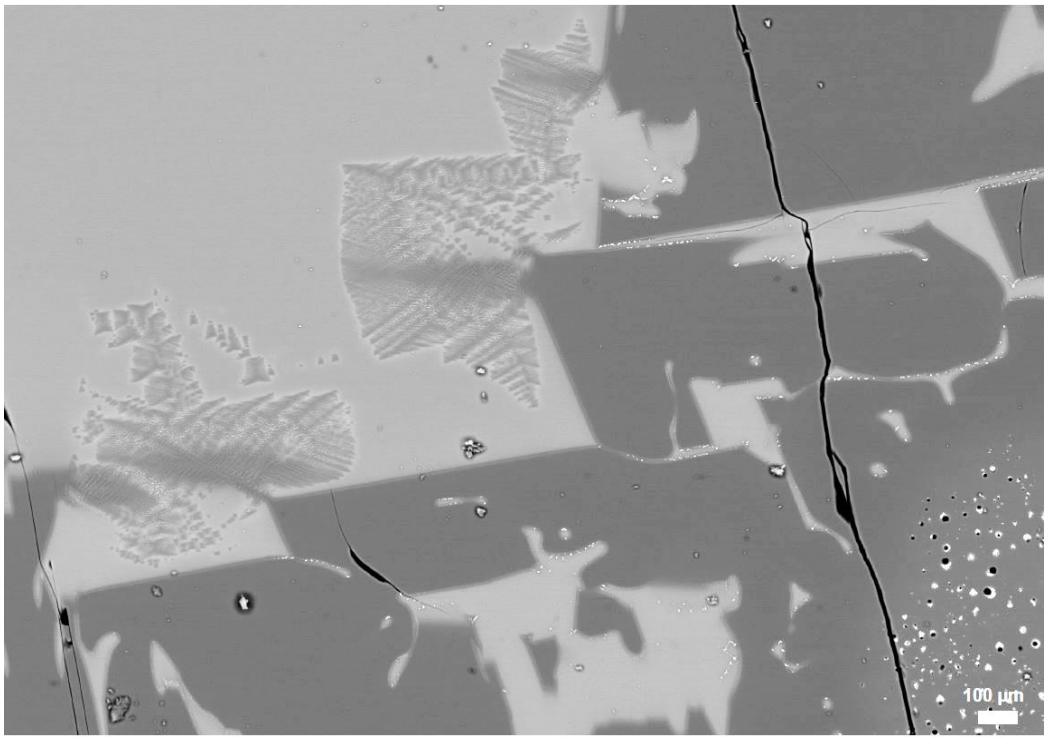

Figure 18. Run 149. BSE image of feather texture from a fine and large-grained sample heated for ten minutes at the liquidus and cooled at 3000 K/hr. Scale bar is 100 µm.

Barred- Barred textures here are those that consist of parallel plates of olivine set within a preferred orientation similar to barred olivine chondrules (Figure 19). All of the barred textures here contain a combination of spinifex, chain, and/or plate morphologies.

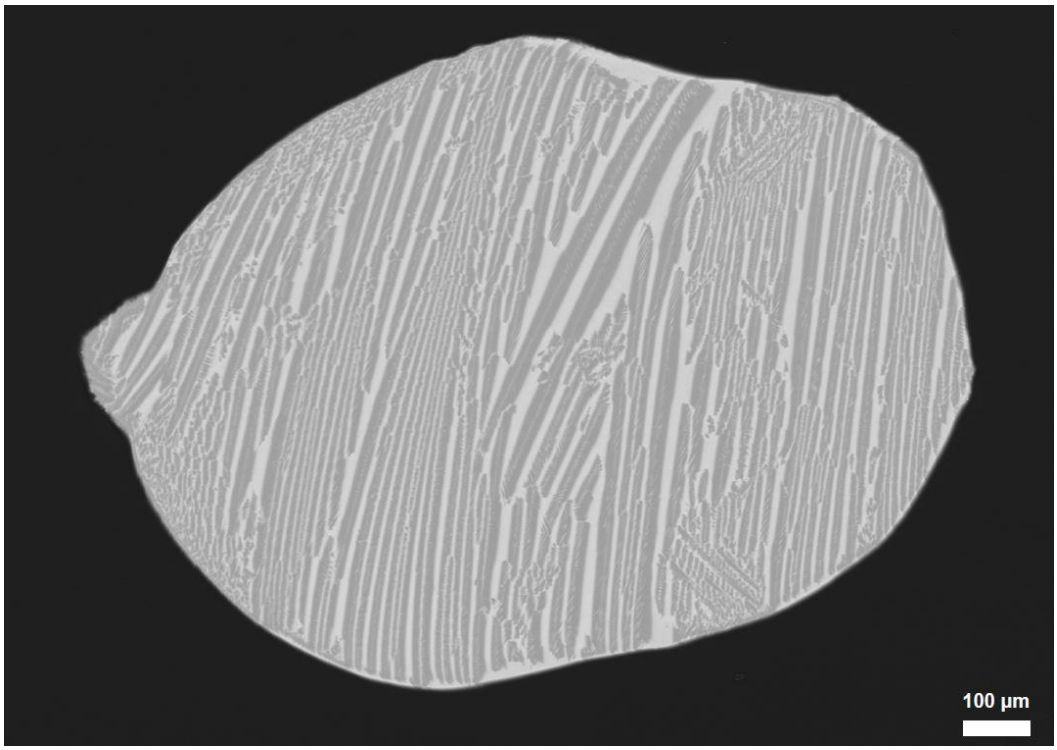

Figure 19. Run106. BSE image of barred texture from a fine and large-grained sample heated for ten minutes at the liquidus and cooled at 5000 K/hr. Scale bar is 100 µm.

Radial- Radial textures consist of fine plates of olivine that radiates from one or more nucleation points. Radial morphologies create a fan-like or shell-like shape (Figure 20).

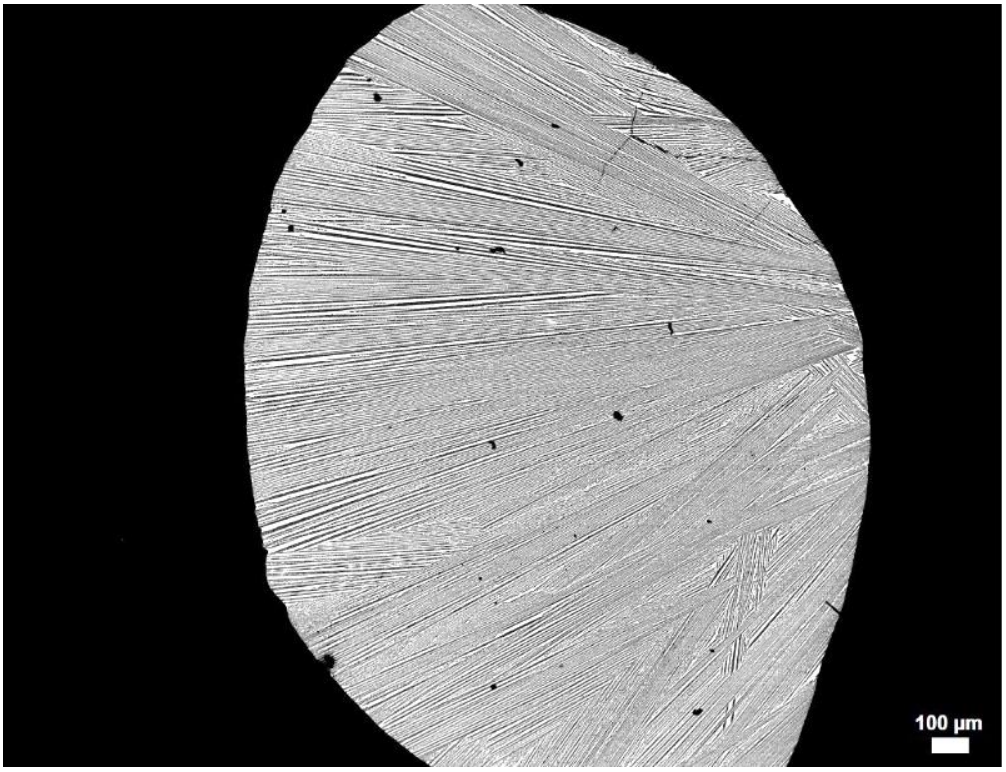

Figure 20. Run 174. BSE image of classic radial texture from an all fine-grained sample heated for one minutes 50 K above the liquidus and cooled at 1000 K/hr. Scale bar is 100 µm.

Porphyritic- Porphyritic-like textures are classified as having subhedral to euhedral grains. The majority of the experimentally reproduced textures contain skeletal rim growth and hopper morphologies, which are still classified as porphyritic-like (Figure 21). Very few results show textures consistent with classic porphyritic chondrules, which will be described more in detail in the Discussion chapter.

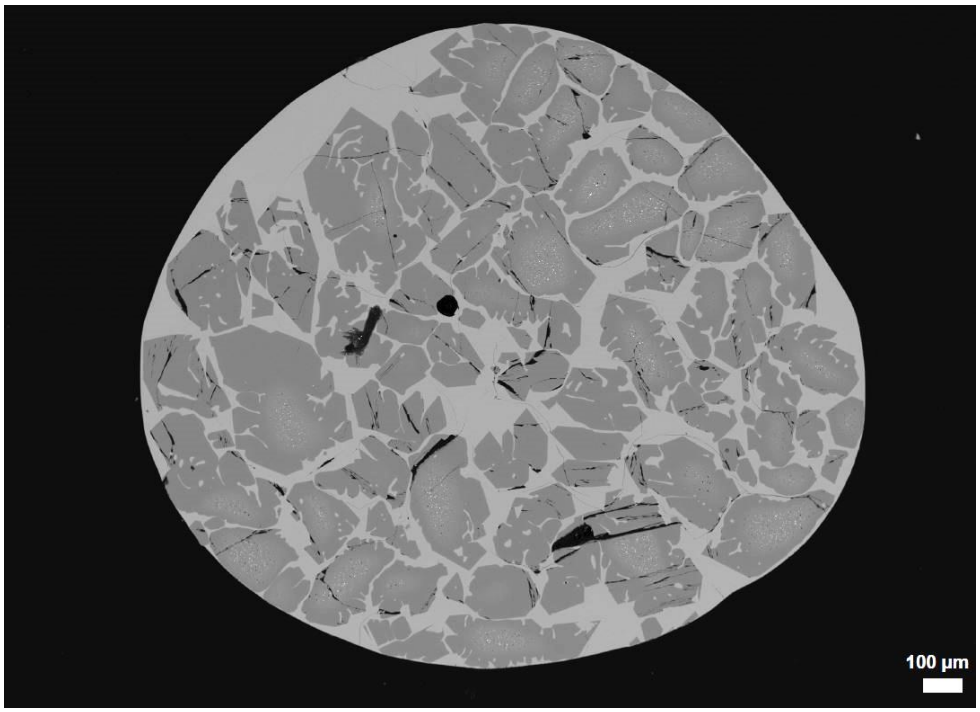

Figure 21. Run 200. BSE image of porphyritic texture from an all fine-grained sample heated for one minute 50 K above the liquidus and cooled at 600 K/hr. Scale bar is 100 µm.

Transitional- Transitional textures are defined here as having a combination of barred or porphyritic textures (Figure 22).

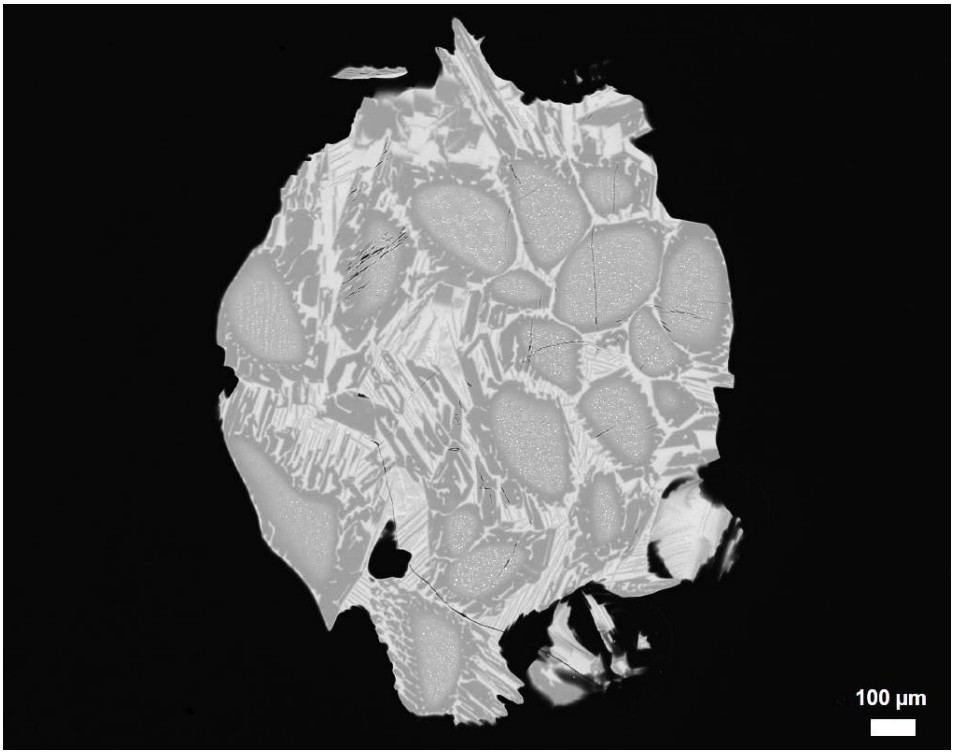

Figure 22. Run 107. BSE image of transitional texture from a fine and large-grained experimental fun heated for 5 minutes at the liquidus and cooled at 5000 K/hr. v

Results by Cooling Rate

We conducted a total of 133 experimental runs exploring a variety of parameter combinations, with 123 successful runs showing observable textures including glass (see Table A1 in the Appendix). 10 experiments were unsuccessful and therefore could not be analyzed. In the ten failed experiments, the experimental charges dropped off of the Pt wire basket during melting and were lost. The textures are classified into four main

categories based on natural chondrule textures: radial, barred, transitional, and porphyritic. The experimental runs resulting in glassy textures are listed in Table 5.

Table 5. Experimental results yielding glassy textures. Glass textures are predominantly reproduced at peak temperatures 50 K above the liquidus at longer heating durations.

Sample	Grain Size	Peak Temperature (K)	Heating Duration (min)	Cooling Rate (K/hr)
202	FF	1608	1	600
197	FL	1608	5	600
191	FF	1608	10	600
95	FL	1608	10	1000
166	FL	1658	10	1000
180	FF	1658	10	1000
113	FL	1608	10	3000
181	FF	1658	1	3000
168	FL	1658	10	3000
145	FF	1658	10	3000
112	FL	1558	10	5000
114	FF	1608	10	5000
104	FL	1608	10	5000
164	FL	1658	1	5000
162	FF	1658	5	5000
163	FF	1658	10	5000
143	FL	1658	10	5000

FF: albite + diopside + olivine (63 – 90 μm)
FL: albite (63 – 90 μm) + diopside (63 – 90 μm) + olivine (212 – 250 μm)

Radial textures observed here consist of very fine-grained laths of olivine (< 10 microns in thickness) that radiate from at least one point within the chondrule analog. Barred-textures consist of parallel oriented laths of olivine that are greater than 10 microns in thickness. Porphyritic-like textures consist of olivine grains with more anhedral to subhedral shapes showing skeletal rim growth. Such grains typically contain relict cores with Fe oxide blebs. These grains are classified as porphyritic-like as they are

not showing the classical subhedral to euhedral grain morphologies seen in natural chondrules, but they are showing more of a resemblance toward such textures as compared to the other results. Porphyritic textures are defined here as grains with more subhedral olivine grains. Despite the presence of hopper morphologies, we will show how such features are found in natural chondrules and it is acceptable to deem such experimentally reproduced textures as porphyritic.

Figure 23 shows an overview of the different experimental runs at the three peak temperatures investigated. One-minute heating durations do not yield porphyritic or porphyritic-like textures at the higher cooling rates (3000 - 5000K/hr) that have not been explored in previous studies (Figure 23a) However, such textures are observed at cooling rates under 1000 K/hr. Radial textures were also reproduced at cooling rates under 1000 K/hr. Only barred- and transitional-like textures are reproduced at cooling rates this fast. Similarly, five-minute heating durations show no porphyritic or porphyritic-like textures at the faster cooling rates investigated in this study, but true barred and transitional textures were reproduced (Figure 23b). Porphyritic-like textures were produced at cooling rates < 1000 K/hr but a slight deviation to the left of the graph signifies barred-like features as compared to the experiments that plotted within the shaded bar in the one-heated duration. Radial textures were reproduced at cooling rates < 2100 K/hr and barred textures were reproduced at cooling rates < 1000 K/hr. Radial, barred, and transitional textures are all reproduced at the high-end cooling rates using 10-minute heating durations. Again, no porphyritic or porphyritic-like textures were observed. Radial and barred textures were also observed at cooling rates under 1200 K/hr. No porphyritic

textures were reproduced at 10-minute heating durations (Figure 23c). Porphyritic-like textures showing more barred-like features were reproduced at cooling rates < 2400 K/hr.

1-minute

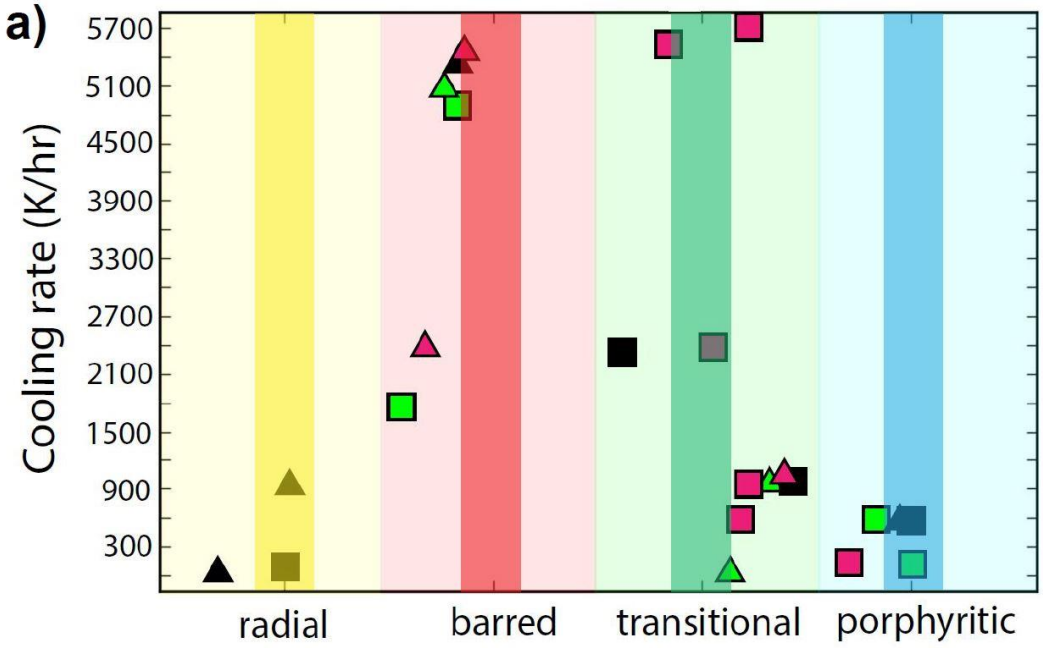

5-minute

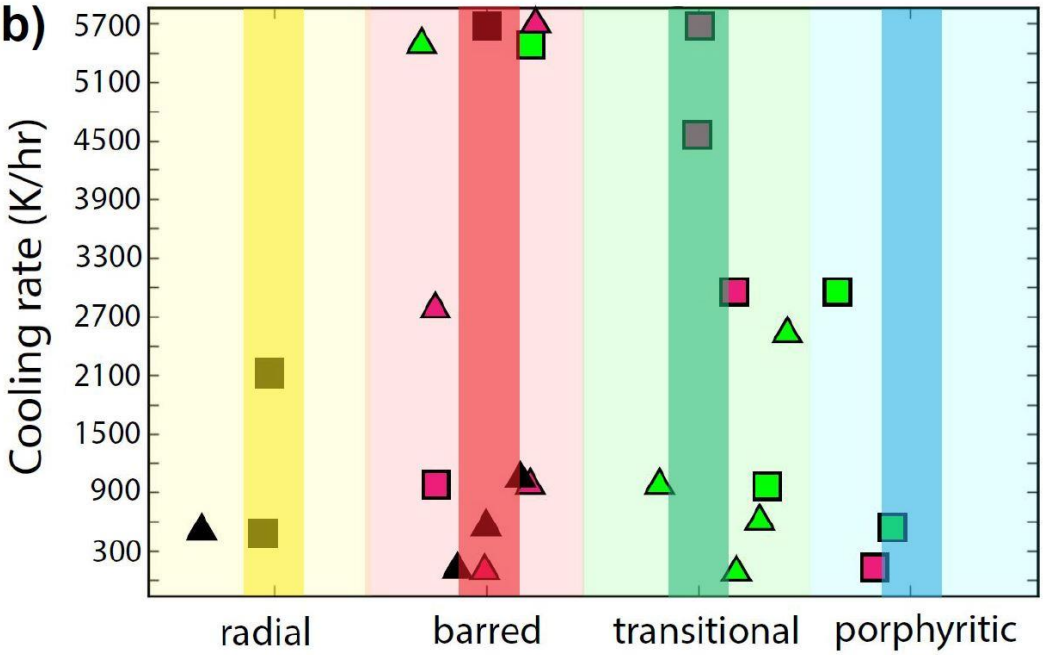

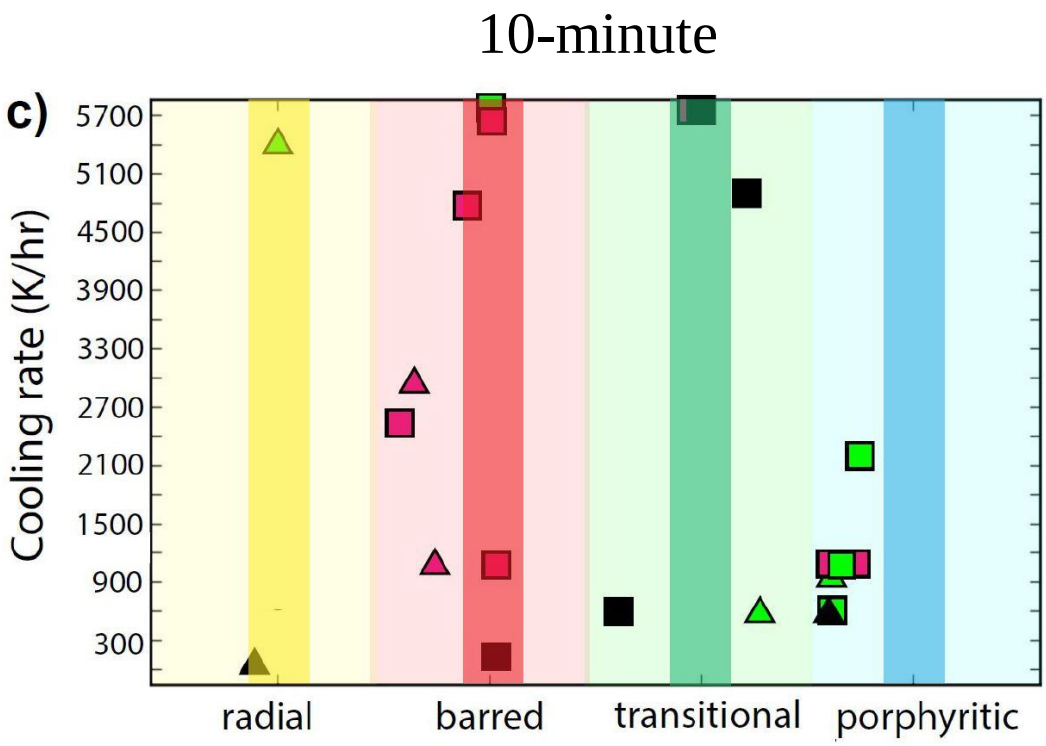

Figure 23. Experimental runs resulting in radial, barred, transitional, or porphyritic textures. Each symbol represents a different experimental run. Shapes denote grain size (triangles are "FF": 63-90 μm albite + diopside + olivine; squares are "FL": 63 – 90 μm albite + diopside, and 212 – 250 μm olivine). Symbol colors denote peak temperature (green is 50 K below the liquidus, red is at the liquidus, and blue is 50 K above the liquidus, where the calculated liquidus is 1608 K). Runs are plotted along the vertical axis by the controlled cooling rates, and along the horizontal axis by the resultant texture (radial textures in the yellow region, barred textures in the red region, transitional textures in the green region, porphyritic textures in the blue region). Runs plotted in the darkest part of each region match the "true" chondritic texture of that type. Deviations to the right of the darker bars demonstrate more porphyritic-like textures and deviations to

the left of the bars demonstrate more barred-like textures. Transitional textures are defined here as a texture exhibiting both relict cores and spinifex textures. No “true” porphyritic textures are reproduced using heating duration of 10 minutes. Porphyritic textures are reproduced with heating durations of 1 and 5 minutes, with cooling rates no greater than 600 K/hr.

5000 K/hr

The results presented here show a continuum of textures at 5000 K/hr cooling rates. Textural features in these experiments include chain, plate, feather, hopper, dendritic, spinifex, and glass. Relict cores with skeletal rim growths were also observed as well as the intermediate texture between barred and porphyritic defined here as transitional. The dominant chondrule textures present included barred and radial. The desired porphyritic texture was not observed at these faster cooling rates. Table 6 shows an overview of the 5000 K/hr experimental runs at the different peak temperatures investigated for the different heating durations. BSE images of selected runs (in bold in Table 6) are shown in Figure 24. Barred-like textures are both present during 1- and 10 - minute heating durations and nearly identical transitional textures are present at both 5 - and 10 - minute heating durations.

Table 6. Experimental runs using cooling rate of 5000 K/hr.

Peak Temperature (K)	**1 min**	**5 mins**	**10 mins**	**15 mins**
1558	**123**, 125*	121*, 124	112, **119**, 122*	

1608	108, 126*, 140	**107**, 127*, 139	104, 106, 109, 110, 114*, 138	141
1658	161*, **164**	162*, 165	**111**, 143, 147, 163*	

* experimental runs using all fine-grained size fractions

Bold experimental runs are pictured in Figure 24

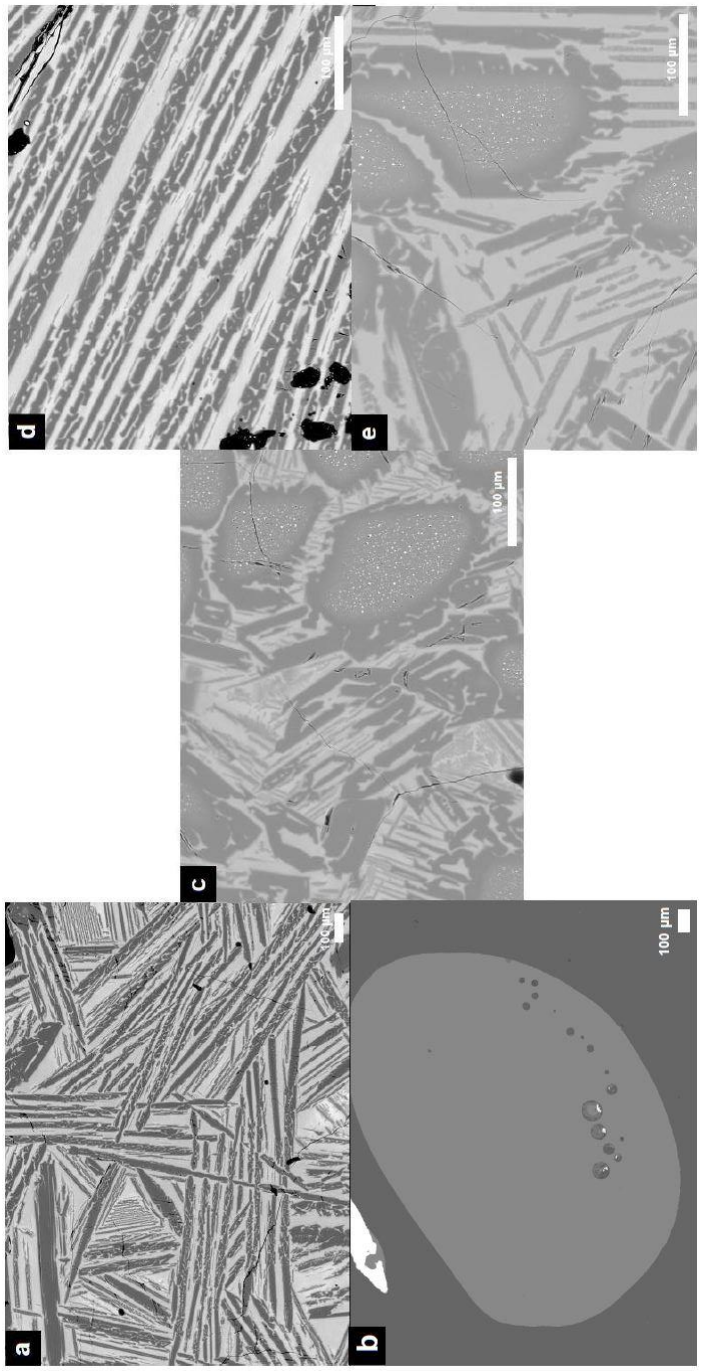

Figure 24. BSE images for experimental runs cooled at 5000 K/hr. a) Run 123: 1 min, FL, L - 50; b) Run 164: 1 min, FL, L + 50; c) Run 107: 5 mins, FL, L; d) Run 119: 10 mins, FL, L - 50; e) Run 111: 10 mins, FL, L + 50. Glass experimental run (b) shows no observable textures. Scale bars are 100 µm.

3000 K/hr

Textural features seen in the 3000 K/hr experiments are similar to those observed in the 5000 K/hr runs and include chain, plate, feather, hopper, dendritic, spinifex, and glass. Relict cores with skeletal rim growths were observed as well as transitional textures. “True” chondrule textures were not easily identified at this cooling rate. Again, the desired porphyritic texture was not observed at this particular cooling rate. Table 7 shows an overview of the 3000 K/hr experimental runs at the different peak temperatures investigated for the different heating durations. BSE images of selected runs (in bold in Table 7) are shown in Figure 25. Barred-like textures dominated the experimental runs despite the different parameter combinations used. However, experimental runs such as those from Run 153 show a transitional-like texture with an increase in relict cores.

Table 7. Experimental runs using cooling rate of 3000 K/hr

Peak Temperature (K)	**1 min**	**5 mins**	**10 mins**
1400	69, 70, 71		
1558	151*, **178**	155, 167*	150
1608	154, 183*	**153**, 182*	113, **132**, 148*, 149
1658	**152**, 181*	176*, 179	145*,**168**

* experimental runs using all fine-grained size fractions

Bold experimental runs are pictured in Figure 25

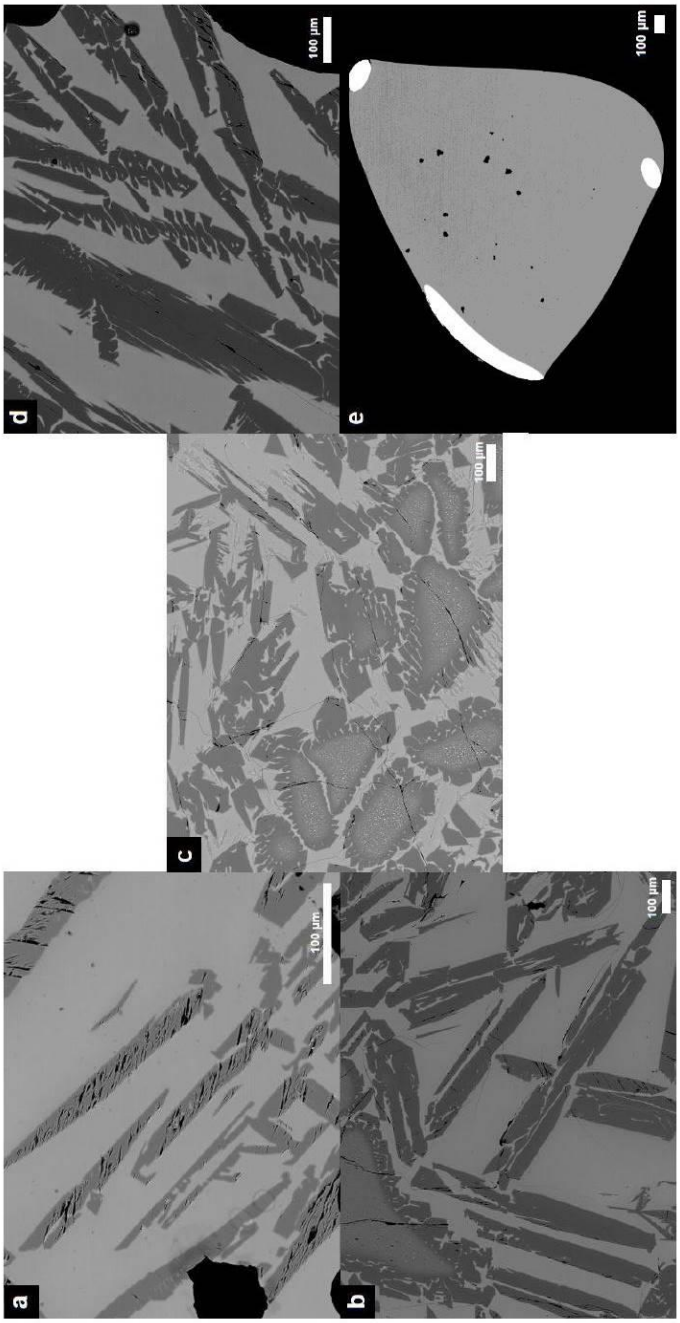

Figure 25. BSE images for experimental runs cooled for 3000 K/hr. a) Run 178: 1 min, FL, L - 50; b) Run 152: 1 min, FL, L + 50; c) Run 153: 5 mins, FL, L; d) Run 132: 10 mins, FL, L; e) Run 168: 10 mins, FL, L + 50. Glass experimental run show no observable textures. Scale bars are 100 µm.

1000 K/hr

Textures observed at 1000 K/hr cooling rates include chain, plate, feather, hopper, spinifex, and glassy, as well as relict cores with skeletal rim growth similar to both the 5000 and 3000 K/hr experiments. As seen with the higher cooling rates, these experiments show both radial and barred textures. No dendritic textures were observed. However, a noticeable difference is the increase in transitional textures as well as the presence of porphyritic-like textures at this cooling rate. Table 8 shows an overview of the 1000 K/hr experimental runs at the different peak temperatures investigated for the different heating durations. BSE images of selected runs (in bold in Table 8) are shown in Figure 26. At peak temperatures lower than the liquidus (1558 K), results show olivine fragments, but skeletal growth around the rims of the grains is starting to become apparent despite a heating duration of 1 minute.

Table 8. Experimental runs using cooling rate of 1000 K/hr

Peak Temperature (K)	**1 min**	**5 mins**	**10 mins**	**15 mins**	**20 mins**
1400	61, 62, 63, 85	91	74, 77, 82, 83, 87, 92	80	78, 79
1558	**98**, 160*	169*, 170	**144***, 156		
1608	97, 191*, 173	96, **129**, 172*	95, 105, 131, 133*, 142		
1658	174*, **177**	175*	**166**, 180*		

* experimental runs using all fine-grained size fractions

Bold experimental runs are pictured in Figure 26

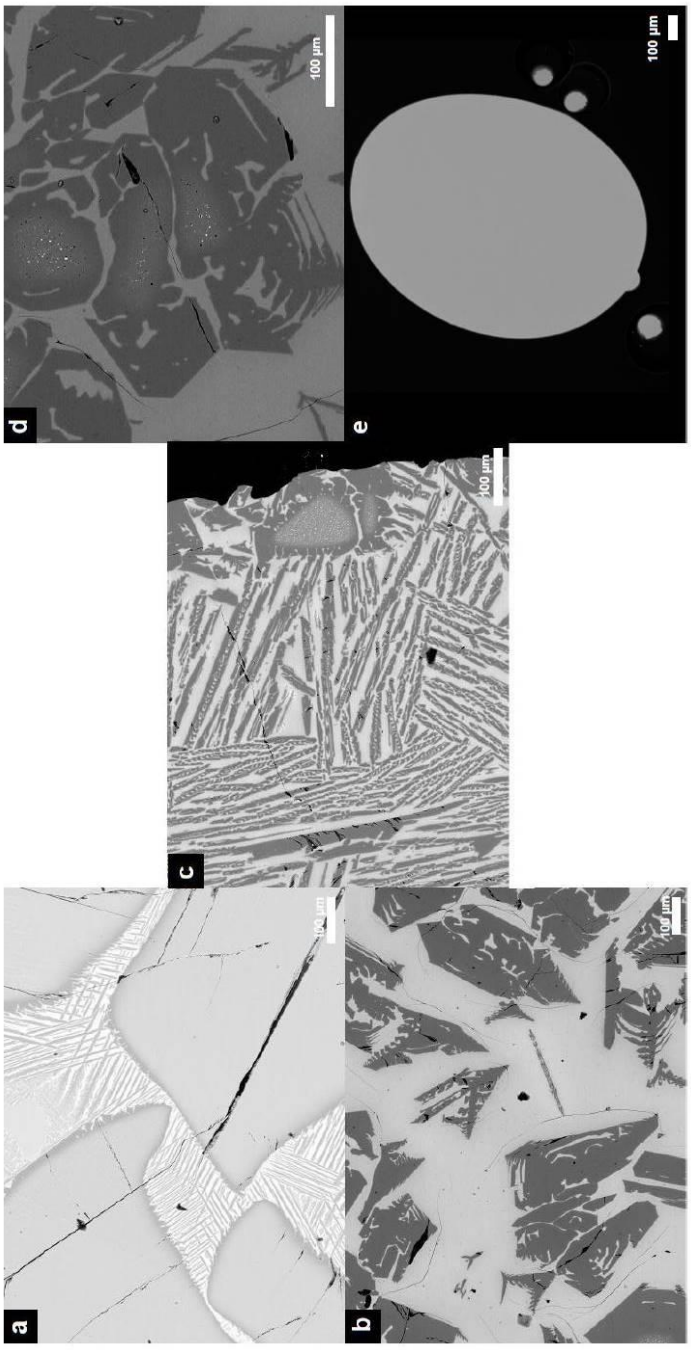

Figure 26. BSE images for experimental runs cooled for 1000 K/hr. a) Run 98: 1 min, FL, L - 50; b) Run 177: 1 min, FL, L + 50; c) Run 129: 5 mins, FL, L; d) Run 144: 10 mins, FF, L - 50; e) Run 166: 10 mins, FL, L + 50. Glass experimental run show no observable textures. Scale bars are 100 µm.

600 K/hr

600 K/hr cooling rates yield similar olivine morphologies as those previously seen in the 5000, 3000, and 1000 K/hr experimental runs. However, true porphyritic textures were observed for the first time at this cooling rate. The porphyritic textures exhibit few subhedral to euhedral grains with hopper morphologies. Both barred and radial textures were also reproduced at 600 K/hr. Table 9 shows an overview of the 600 K/hr experimental runs at the different peak temperatures investigated for the different heating durations. BSE images of selected runs (in bold in Table 9) are shown in Figure 27.

Table 9. Experimental runs using cooling rate of 600 K/hr

Peak Temperature (K)	**1 min**	**5 mins**	**10 mins**
1558	**192**	205, 206*	193*, **194**
1608	202*, 204*	**197**	190, 191*
1658	**198**, 200*, 201*	199*, 195, 196*	**188**, 189*

* experimental runs using all fine-grained size fractions

Bold experimental runs are pictured in Figure 27

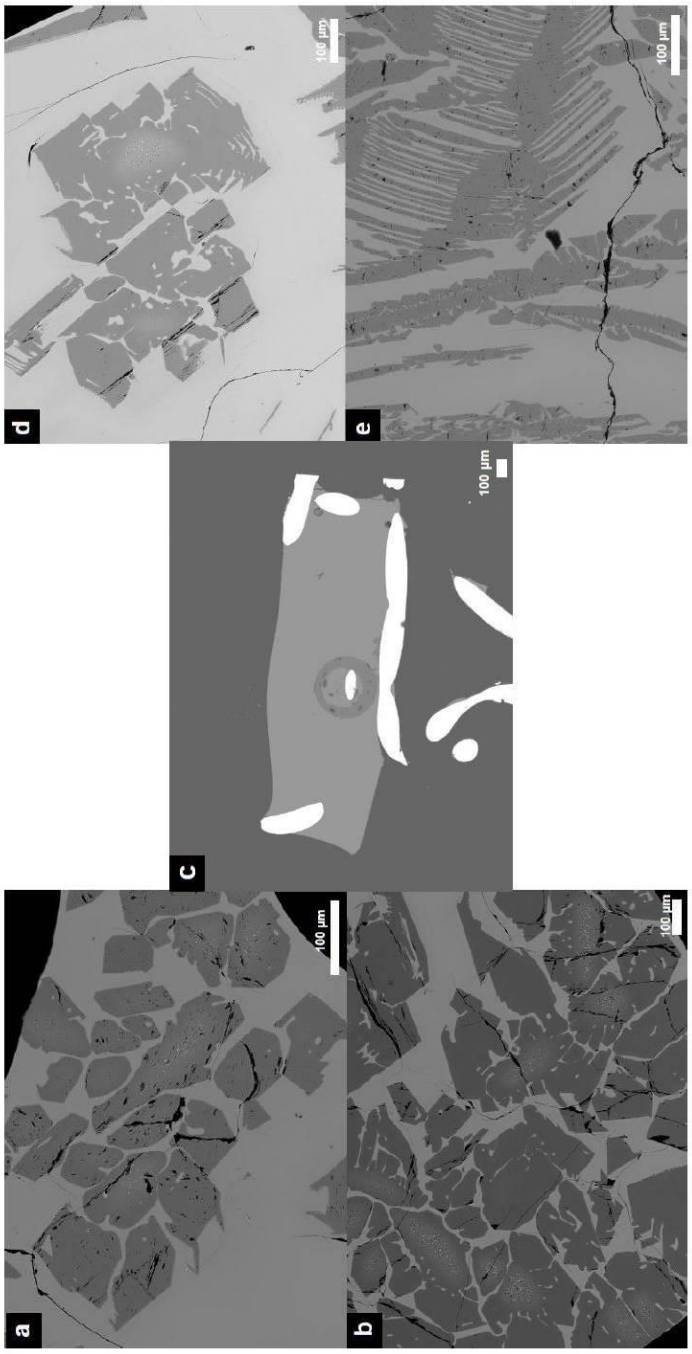

Figure 27. BSE images for experimental runs cooled for 600 K/hr. a) Run 192: 1 min, FL, L - 50; b) Run 198: 1 min, FL, L + 50; c) Run 197: 5 mins, FL, L; d) Run 194: 10 mins, FL, L - 50; e) Run 188: 10 mins, FL, L + 50. Glass experimental run (c) show no observable textures. Scale bars are 100 µm.

300 K/hr

300 K/hr cooling rates show similar textural features as those seen in the 600 K/hr runs. True porphyritic textures were also observed showing few subhedral to euhedral grains with hopper morphologies. Both barred and radial textures were also reproduced at 300 K/hr. However, as compared to the 600 K/hr experiments, there were few transitional textures reproduced. Textures were either defined as radial, barred, or porphyritic-like to porphyritic. Table 10 shows an overview of the 300 K/hr experimental runs at the different peak temperatures investigated for the different heating durations. BSE images of selected runs (in bold in Table 10) are shown in Figure 28.

Table 10. Experimental runs using cooling rate of 300 K/hr

Peak Temperature (K)	**1 min**	**5 mins**	**10 mins**
1558	**214**, 218*	224*	212*, **223**
1608	208*, 222	209*, **219**	207*, 210*, 215
1658	211*, **221**	220*	**216**, 217*

* experimental runs using all fine-grained size fractions

Bold experimental runs are pictured in Figure 28

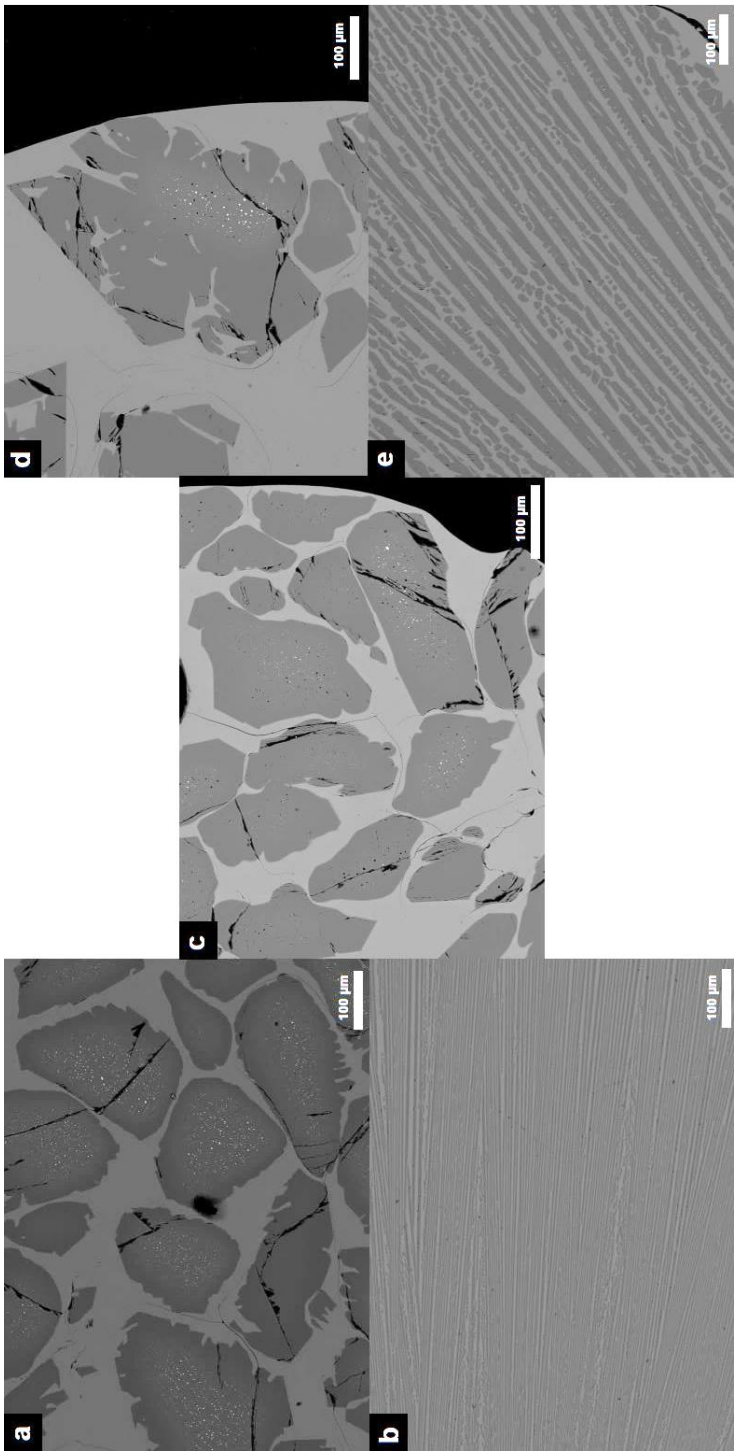

Figure 28. BSE images for experimental runs cooled for 300 K/hr. a) Run 214: 1 min, FL, L - 50; b) Run 221: 1 min, FL, L + 50; c) Run 219: 5 mins, FL, L; d) Run 223: 10 mins, FL, L - 50; e) Run 216: 10 mins, FL, L + 50. Scale bars are 100 µm.

CHAPTER 4

DISCUSSION

Meteoritic vs Experimentally Reproduced Textures

To benchmark the experimentally-produced textures, the experimental images were compared with BSE images of chondrules from Queen Alexandra Range (QUE) 97008, an L3.05 chondrite. This particular chondrite was chosen as it is one of few chondrites to have experienced minimal secondary processing and terrestrial weathering (e.g., Nettles et al. 2006; Berlin et al. 2011). QUE 97008 displays similar quench crystal textures as some of the experimentally reproduced chondrule textures in this work (Figure 29). The majority of the experimentally-produced porphyritic textures here contain both skeletal grains and the classically-defined subhedral to euhedral grains described in porphyritic chondrule textures. However, we found that QUE 97008 contains a few porphyritic chondrules with skeletal textures implying that not all classically-defined porphyritic chondrules are comprised solely of subhedral to euhedral grains, thus making the experimentally reproduced textures here consistent with textures of natural chondrules (Figure 30-31). Such skeletal features of natural chondrules may argue for cooling rates at the high end of the allowed range (up to 600 K/hr), and we observed similar skeletal features investigating cooling rates as high as 5000 K/hr. Connolly et al. (1998) addressed similar conclusions using FeO-rich chondrule analogs. When describing their chondrule analogs, they used HPO (hopper porphyritic olivine and ELHPO (elongate-hopper porphyritic olivine).

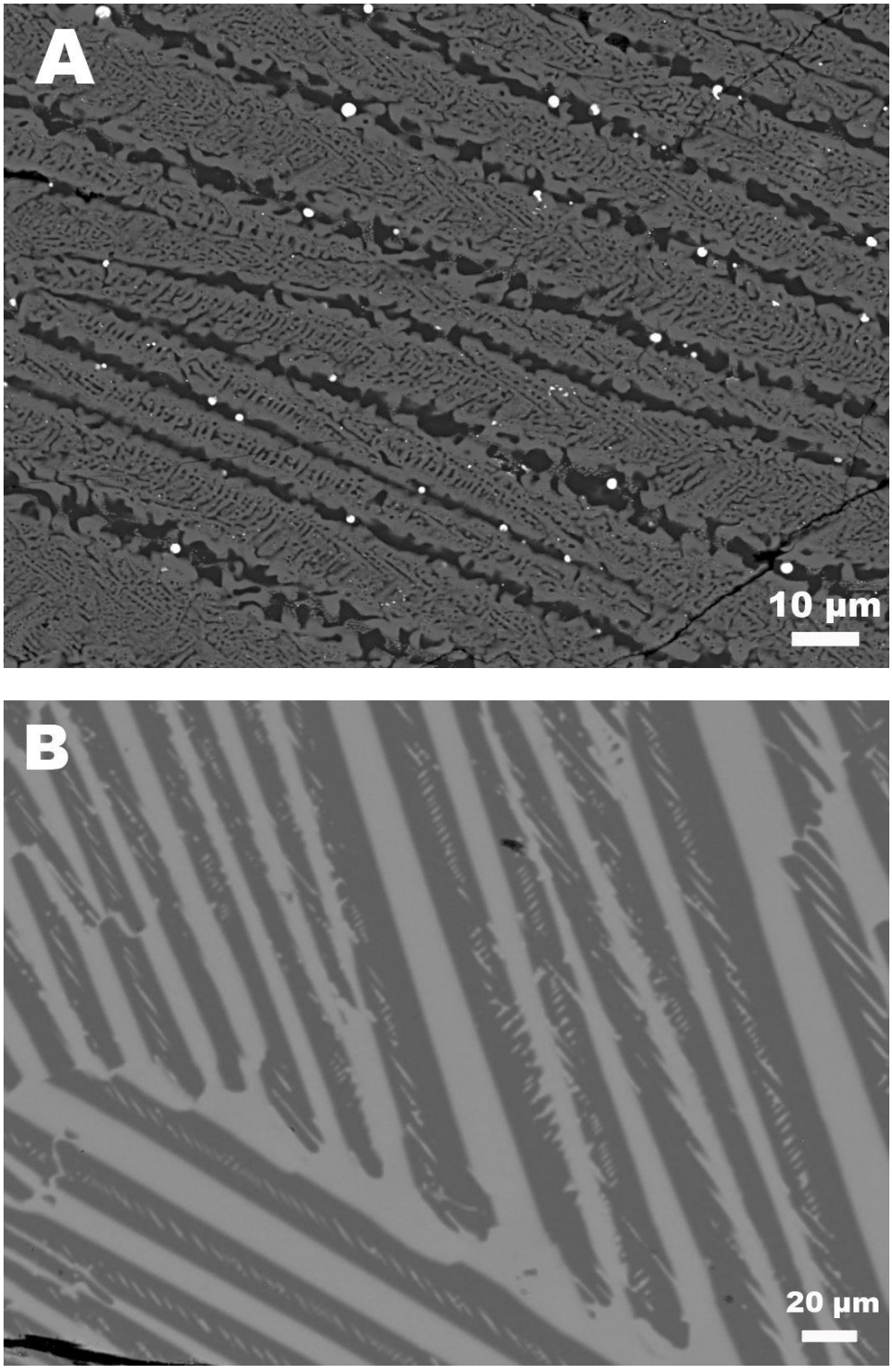

Figure 29. BSE images showing similar quench crystal textures present in both meteoritic (A) and experimentally (B) produced textures using a 600 K/hr cooling rate.

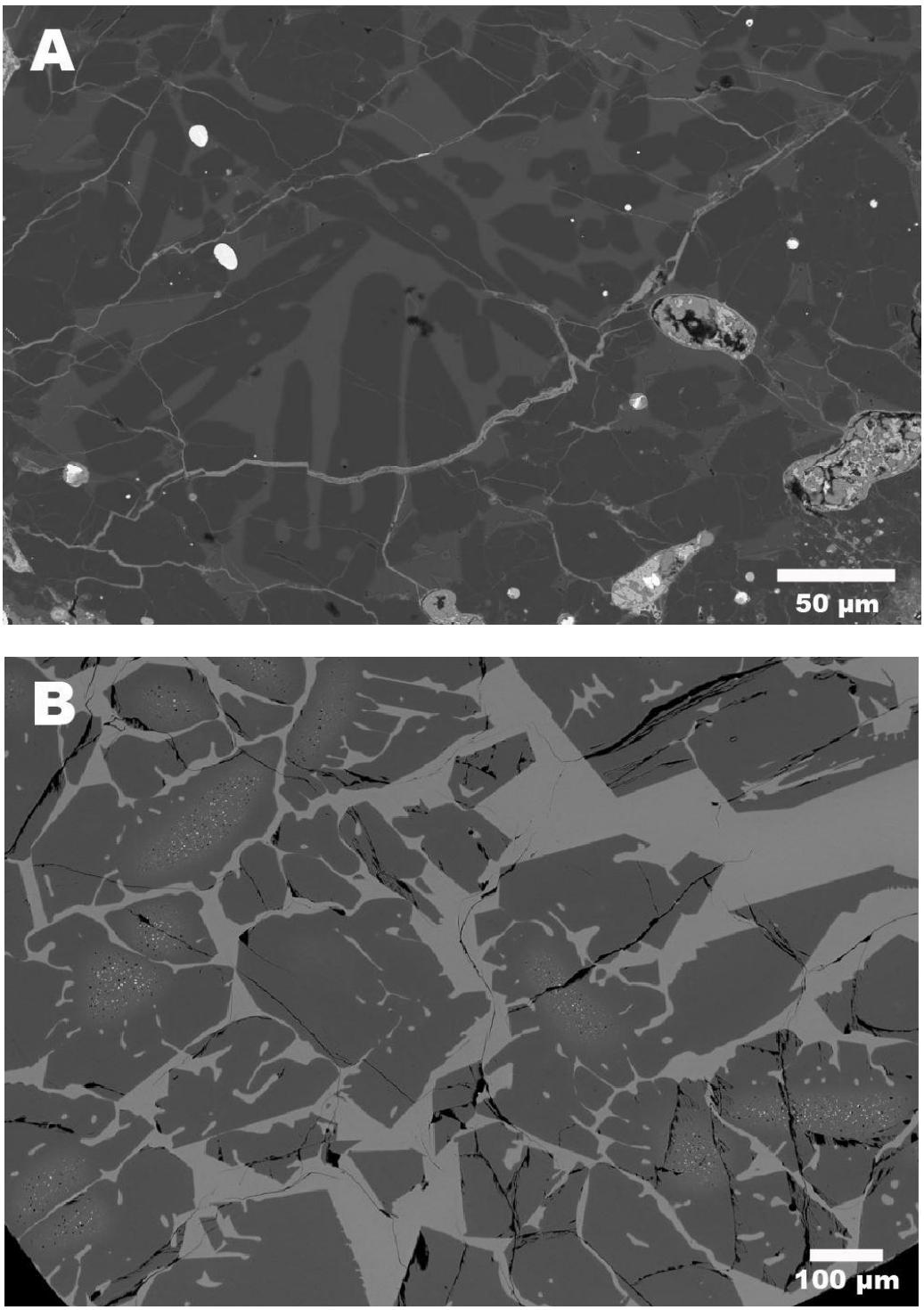

Figure 30. BSE images showing similar skeletal grains present in both meteoritic (A) and experimentally (B) produced textures using a 600 K/hr cooling rate.

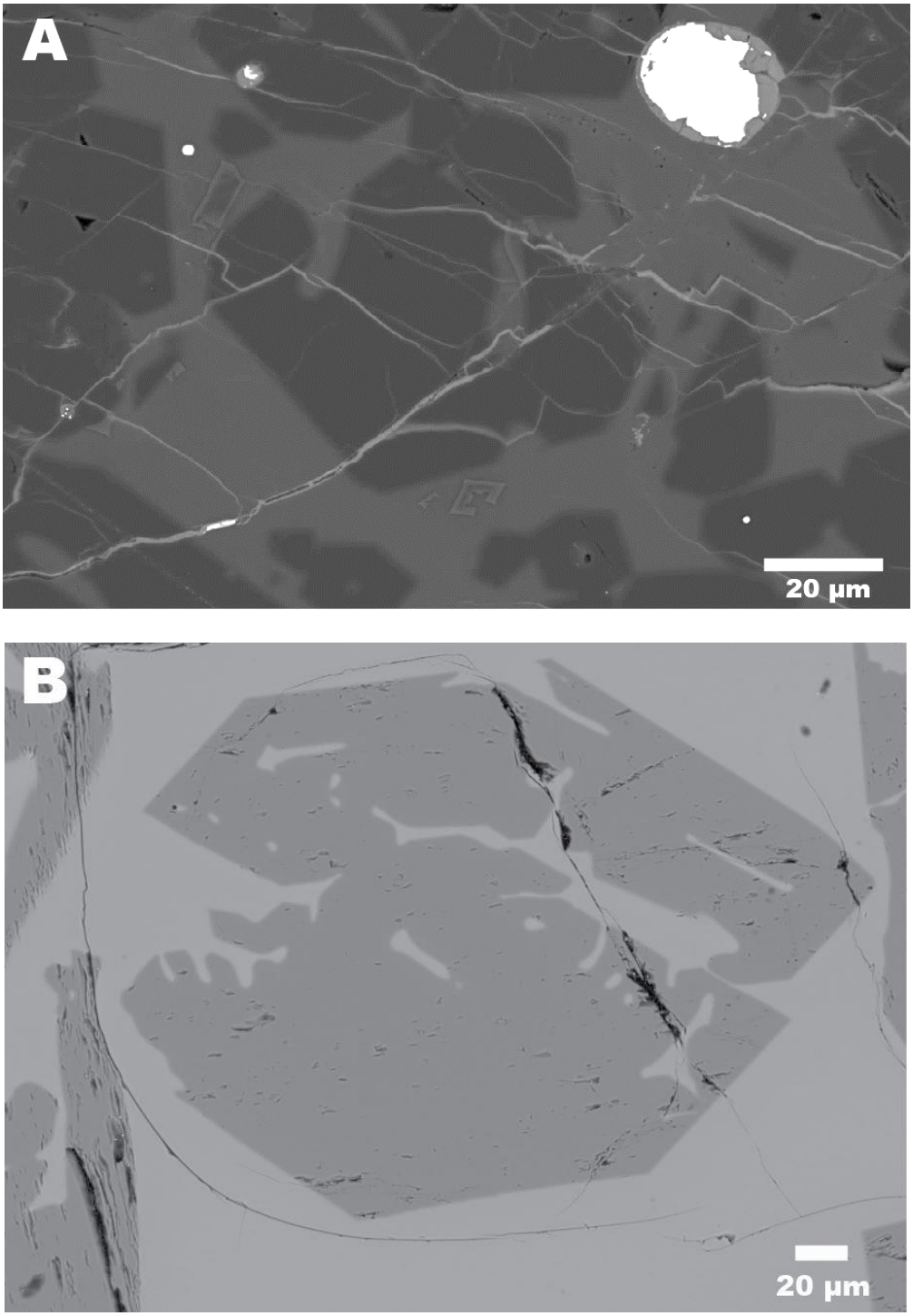

Figure 31. BSE images showing s similar skeletal grain present in both meteoritic (A) and experimentally (B) produced textures using a 600 K/hr cooling rate.

Constraining Heating Duration

In these experiments, only heating durations ≤ 10 min were examined. This was motivated in part by constraints from retention of moderate volatiles like Na, which would have been lost by evaporation within only minutes at temperatures above the liquidus (Yu & Hewins 1997) and requires cooling rates ~ 10^4 K/hr at temperatures above the liquidus. However, this constraint is complicated by the finding of Alexander et al. (2008) that substantial Na also existed in the melt during the slower (cooling rates < 10^3 K/hr) crystallization stage of at least some chondrules. They inferred high partial pressures of Na vapor in the chondrule formation environment, in which case Na retention at high temperatures potentially could be explained by high Na partial pressures instead of short heating durations, although short heating durations are not excluded. The exploration of heating durations ≤ 10 min in this thesis work was also motivated by constraints from chemical dissolution. The size distribution of anhedral grains within low-Ca pyroxene suggests that olivine within chondrules suffered from dissolution during chondrule formation (Soulié et al. 2017), suggesting that grain dissolution could be used as an independent method to constrain the heating durations required to preserve olivine grains.

Soulié et al. (2017) recently explored olivine dissolution rates in chondrule-like melts using X-ray computed microtomography analyses to measure the sizes of grains. In chondrule-like melts with bulk composition similar to our experimental analogs and a calculated liquidus of 1319 K, at peak temperatures between 1456 K – 1531 K they measured grains to be dissolving at rates 7 - 17 μm/min. This implies that preservation of ~100 μm radius olivine grains requires short exposure times (6 – 14 minutes) at high

temperature, implying fast cooling rates through the crystallization range ~10^3 K/hr. The experiments presented here indicate that the dominant porphyritic textures are only reproduced at cooling rates under 1000 K/hr, favoring lower cooling rates. This is the motivating factor to repeat the analysis of Soulié et al. (2017) for the experimental samples.

To calculate dissolution rates for the experiments, 29 representative grains with relict cores from BSE images of 5 samples with cooling rates consistent with porphyritic textures (< 1000 K/hr) were selected. These are listed in Table 11. The final radius of each grain was measured in the long axis of the relict cores, neglecting skeletal rim growth. It is assumed that each grain had initial radius R_{init} = 106 μm based on the initial starting grain size fractions used in the chondrule analogs. The final grain size is the average radius of grains in that run. The dissolution rate for each grain is then calculated as the change in grain radius divided by the known heating duration time, as follows:

$$\frac{dr}{dt} = \left|\frac{\Delta R}{\Delta t}\right| = \frac{\bar{R}_{\mathrm{init}} - \bar{R}_{\mathrm{final}}}{(\mathrm{t}_{\mathrm{final}} - \mathrm{t}_{\mathrm{init}})} \qquad \text{(eqn. 2)}$$

Table 11. Summary of selected grains used to determine dissolution rates. All of the experimental runs shown consist of FL chondrule analogs. In each run we assume the initial grain size was 106 μm.

Run	T (K)	Cooling Rate (K/hr)	Heating Duration (min)	# Relict Cores	# Relict Cores Measured	Average Core Radius (μm)
214	1558	300	1	47	7	115 ± 5
223	1558	300	10	4	4	94 ± 6

192	1558	600	1	6*	6	45 ± 2
205	1558	600	5	77	8	129 ± 6
194	1558	600	10	4	4	108 ± 6

*Experimental runs starting off with such a small number of relict cores and then showing a significant increase after a few minutes is not typical. Errors shown are 1σ.

For example, let's compare Runs 214 and 223. The experimental products are shown in Figure 32. In Run 214, 47 relict cores were counted, with average grain radius 115 ± 5 μm (the uncertainty is one standard deviation in the range of measured sizes). This is a reasonable estimate of the initial amount of grains that were present at 1 minute in the similar Run 223 with the longer heating durations of 10 minutes. At the end of that run, only 4 relict grains remained, with an average grain radius of 94 ± 6 μm. It is therefore assume that about 43 grains shrank by more than 115 μm in 9 minutes, at an average dissolution rate > 12.8 μm/min, and about 4 grains shrank by about 21 μm, at an average dissolution rate 2.3 μm/min. Altogether the average dissolution rate is > 11.9 ± 0.5 μm/min.

Likewise, in Run 205, with heating duration 5 minutes, 77 relict cores were counted, with an average grain radius of 129 ± 5 μm. This is a reasonable number of particles at 5 minutes into Run 194, which after 10 minutes had 4 relict cores with average radius 108 ± 5 μm. The surviving grains experienced average dissolution rate 4.2 ± 0.2 μm/min, while the average dissolution rate overall was > 24.6 ± 1.2 μm/min. A ranged of dissolution rates is inferred, with some (up to ~10%) of grains experiencing low dissolution rates ~ 2 – 4 μm/min, but the majority experiencing dissolution rates in excess

of 12 – 25 μm/min. These rates compare favorably with the rates 7 – 17 μm/min found by Soulie et al. (2017).

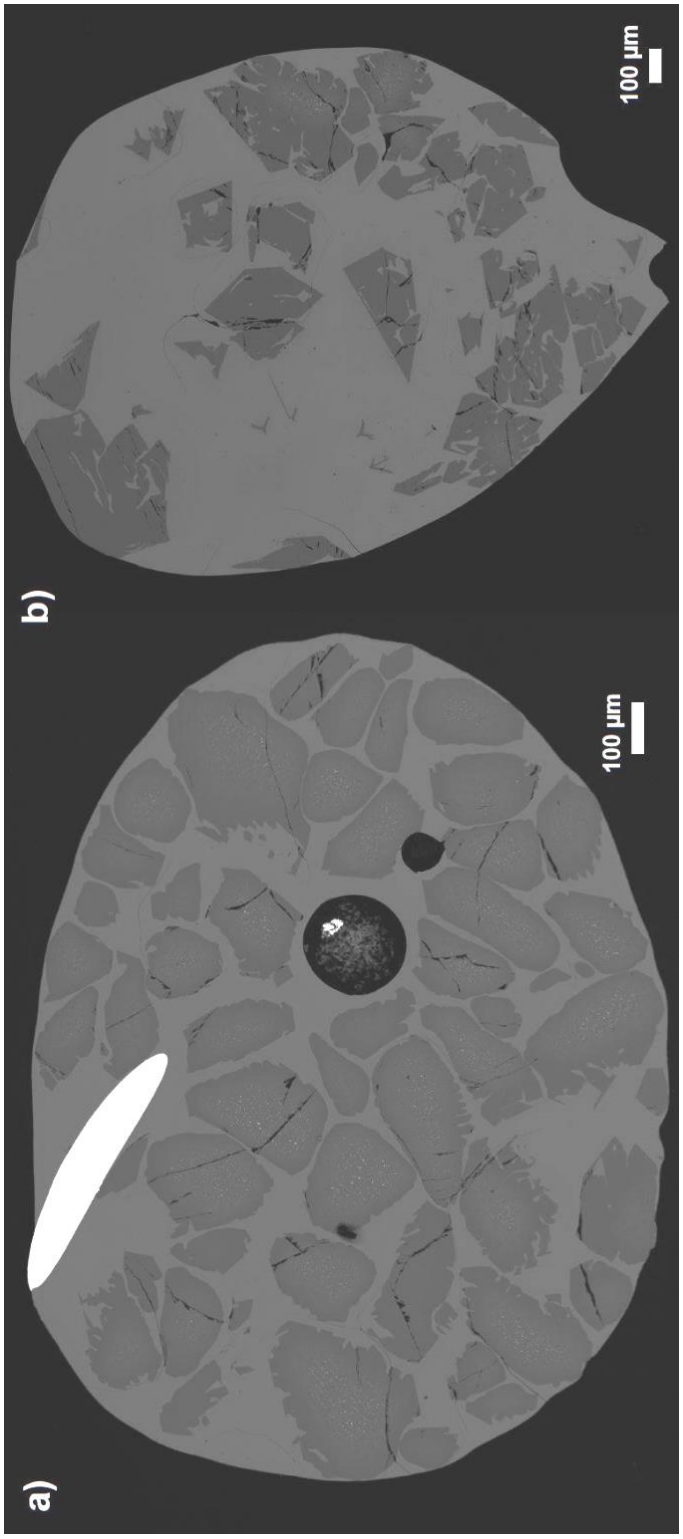

Figure 32. BSE images 300 K/hr experimental runs. a) Run 214 is heated for 1 minute, after which 47 relict cores remain. The white artefact is a piece of the Pt wire used to

suspend the chondrule analog from the thermocouple. b) Run 223 is heated for 10 minutes after which only 4 relict cores survive. These results imply that between 1 and 10 minutes, about 43 relict grains have dissolved or completely lost their cores. Scale bar is 100 μm.

Porphyritic textures require preservation of hundreds to thousands of relict grains to provide nucleation sites (Desch et al. 2012). In a chondrule with radius 300 μm, the maximum size of ~300 such relict grains must be < 50 μm. Preservation of most relict grains of this size would require a heating duration $\Delta t < 2 - 4$ min using chemical dissolution rates 12 – 25 μm/min. About 10% of grains may experience slower dissolution rates 2 – 4 μm/min, but to retain ~ 300 relict grains would require starting with more (~ 3000) grains of smaller size, ~ 25. The heating duration would be limited to $\Delta t < 6 – 10$ min. It is concluded from these chemical dissolution rates that porphyritic textures demand heating durations < 10 minutes.

There are difficulties in using chemical dissolution to constrain heating durations. From Table 8, Run 192, with identical parameters as Runs 205 and 194, had fewer and smaller relict grains after 1 minute than Runs 205 and 194 did after 5 and 10 minutes of heating. This suggests that otherwise similar runs might not be compared, and some unknown factor may be accelerating the dissolution of relict grains. Nevertheless, it is considered a robust result that porphyritic textures cannot arise in chondrules at peak temperatures, 50 K below the liquidus up to 200 K above the liquidus, for more than about 10 minutes.

Comparison with Previous Studies

Our experimental results investigating cooling rates from 300 - 5000 K/hr in many ways conform with previous studies, summarized in Figure 3. Porphyritic textures are produced at cooling rates up to 600 K/hr and barred and radial textures at cooling rates up to 5000 K/hr. Previous experiments had also reproduced these textures using the cooling rates this study inferred to work, but had also reproduced porphyritic textures at higher cooling rates, up to 2500 K/hr (Lofgren & Russell, 1986). This thesis work was not able to reproduce porphyritic textures at such high cooling rates, due to the different parameters used. Shocks driven by gravitational instabilities are predicted to yield cooling rates as low as 10 K/hr. Cooling rates this low were not investigated, however; Hammer (2006) shows barred textures reproduced as low as 72 K/hr after being heating for 12 hours. Cooling rates lower than this show more anhedral to subhedral grains. This implies a lower bound for barred textures and cooling rates of 10 K/hr may be too slow to reproduce the quench textures observed in natural chondrules.

The most significant difference is in the duration of heating at peak temperature. Lofgren and Russell (1986) in particular reproduced porphyritic textures at 2500 K/hr by heating their samples at peak temperature for 17 hours. The models developed since that time (especially heating by shocks and impacts), reviewed in Chapter 1, predict shorter heating durations of minutes or less, and as reviewed above, chemical dissolution argues for heating durations < 10 minutes. In Figure 33 we reproduce Figure 3 from Desch et al. (2012), shading in gray those experiments that used heating durations much greater than 10 minutes. Only two experimental studies considered such short heating durations. Tsuchiyama et al. (2004) considered short heating durations, but focused on production

of barred olivine textures. The study with the highest cooling rates previously found to successfully reproduce porphyritic textures with short heating durations is that of Connolly et al. (1998).

The study of Connolly et al. (1998) used a very short heating duration (<< 1 minute) and cooled their samples at 500 K/hr. They also considered the effects of grain size on texture, and how a peak temperature at the superliquidus can affect texture. It is noted here that while a porphyritic texture was reproduced at 500 K/hr, what Connolly et al. (1998) classified as porphyritic texture, this work would classify as a transitional texture, due to the co-existence of elongated laths. The paucity of high-resolution images and the lack of a standard nomenclature make it difficult to compare reproduced textures. Connolly et al. (1998) noted that a large number of porphyritic textures they produced exhibited hopper morphologies, a common feature also seen in our experimental results. They also suggest that smaller initial grain sizes may reduce the likelihood of formation of hopper morphologies, making experimentally reproduced porphyritic textures more consistent with the porphyritic textures found in chondrites. These results suggest 500 K/hr is near the maximum cooling rate that can give rise to porphyritic textures. This is in accord with the finding of this thesis work that only cooling rates up to about 600 K/hr reproduce porphyritic textures.

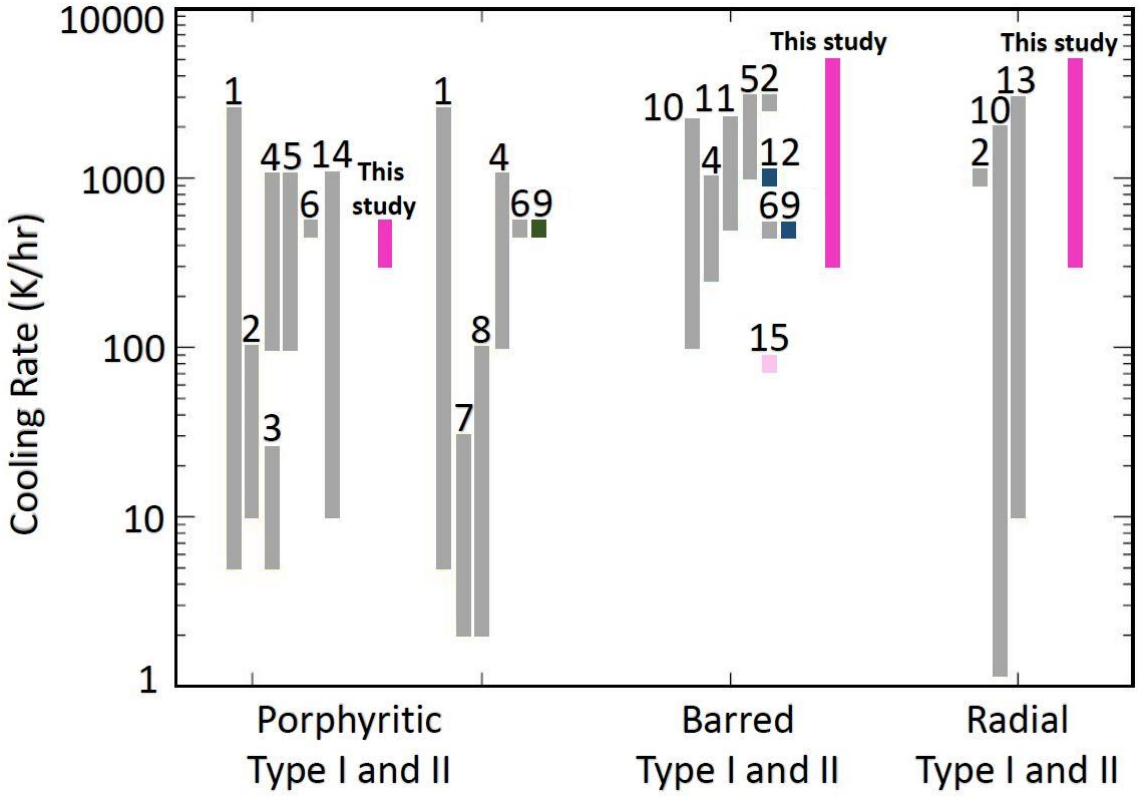

Figure 33. Chondrule textures reproduced by various cooling rates in previous experimental studies. Studies shown in gray include results using heating durations longer than the 10 minutes inferred from chemical dissolution, retention of volatiles, and chondrule formation models. 1. Lofgren and Russell (1986); 2. DeHart and Lofgren (1996); 3. Wick and Jones (2012); 4. Radomsky and Hewins (1990); 5. Lofgren (1989); 6. Connolly and Hewins (1991); 7. Weinbruch and Müller (1995); 8. Jones and Lofgren (1993); 9. Connolly et al. (1998); 10. Kennedy et al. (1993); 11. Lofgren and Lanier (1990); 12. Tsuchiyama et al. (2004); 13. Hewins et al. (1981); 14. Nettles et al. (2005); 15. Hammer (2006). Modified from Desch et al. (2012).

Relationship to the Planetary Embryo Bow Shock Model

As discussed in Chapter 1, the planetary embryo bow shock model tends to predict cooling rates through the crystallization temperature range of thousands of K/hr. Certain cases (e.g., the adiabatic shocks 6 km/s) investigated by Mann et al. (2016) will generate cooling rates in the range 600 – 800 K/hr, assuming a planetary body with radius 3000 km. Cooling rate is inversely proportional to planetary radius, so a slightly larger embryo (e.g., 4000 km radius) could yield lower cooling rates (450 – 600 K/hr), more comfortably consistent with porphyritic textures. According to the results of Mann et al. (2016), only shocks > 6 km/s melt chondrules, while relative velocities between the embryo and nebular gas much above 7 km/s require the embryo's orbit to have eccentricities > 0.2 that are difficult to generate. The cooling rates of chondrules increase slightly with shock speed, being 50% higher for 7 km/s shocks than for 6 km/s shocks (900 – 1200 K/hr instead of 600 – 800 K/hr for the adiabatic shock around a 3000 km-radius embryo). The planetary embryo bow shock model robustly predicts short heating durations (< 10 minutes) and chondrule cooling rates ~ 600 K/hr, with the opportunity for higher cooling rates to be generated. The results presented here show that these would generate porphyritic textures.

Interestingly, these parameters are also consistent with production of barred and radial textures as well. Figure 23 shows that true barred and radial textures are produced with cooling rates ≥ 600 K/hr, if the heating durations are 5-10 minutes and/or the precursors are fine-grained, while true porphyritic textures are produced by the shortest heating durations ~ 1 minute, with coarser-grained precursors. Of course, faster cooling rates >> 600 K/hr would only be consistent with non-porphyritic textures; but even if

bow shocks only generated a narrow range of cooling rates, different chondrule textures could arise from differences in grain size or heating durations.

Further tests of the bow shock model should consider the effects of grain size. The majority of samples produced with porphyritic-like textures contain mostly hopper morphologies using grain size fractions as low as 63 μm, but Connolly et al. (1998) showed that the finest starting materials (< 63 μm) resulted in more porphyritic textures with less hopper morphologies. This could imply smaller grain size fractions could yield less hopper morphologies. However, results from this particular study also show a high abundance of microporphyritic textures reproduced using grain size fractions on the smaller end of those investigated. Future work should include investigating smaller grain size fractions while maintaining similar compositions, heating durations, and peak temperatures, and the effect of the growth of hopper morphologies should be examined more carefully as this is another constraint to further understand chondrule formation as some chondrules contain these morphologies but it is not typical. Schrader et al. (2018) investigated the *in-situ* chemical and O-isotopic compositions of agglomeratic olivine (AO) chondrules in a CR chondrite and inferred the initial grain size of chondrule precursors to be < 1 to 80 μm, equivalent to dust in the early Solar System. Such grain sizes should be investigated in future furnace experiments.

While further work is suggested to better test the planetary embryo bow shock model, this thesis work has shown that the cooling rates it predicts (generally 600 – 800 K/hr for adiabatic shocks and a 3000b – km radius planetary embryo, maybe 450 – 600 K/hr for a larger 4000-km embryo) are consistent with the production of porphyritic textures. Barred and radial textures also could be generated, depending on grain size and

heating durations. This shows that the planetary embryo bow shock model is consistent with all known chondrule properties and is still a viable formation mechanism for the majority of chondrules. Further validation would represent a paradigm shift: if chondrule formation could be safely attributed to planetary embryo bow shocks, this would imply that large planetary embryos were already present and on eccentric orbits during the first few million years of our Solar System's history. Rather than chondrules and chondrites being the building blocks of planets, chondrules would have to be considered by-products of planetary formation. Such evidence exists showing that planet building was already taking place during chondrule formation (Figure 34). Calcium aluminum-rich inclusions (CAIs) are the oldest dated solids in the Solar System and represent time zero on the cosmochemical scale. U-corrected ^{207}Pb-^{206}Pb dating techniques have shown an age of CV CAIs 4567.30 ± 0.16 Myr (Connelly et al., 2012). Hf-W concentrations and isotope data provide an age of chondrules at 3.6 ± 0.6 Myr (Budde et al., 2018) after the formation of CAIs. Schrader et al. (2017) provides a new bound on some of the last chondrules to form with an age of 4.56 ± 0.3 Myr after CAI formation. ^{182}Hf-^{182}W decay systematics provide an upper limit for which Mars accreted approximately 50% of its mass of $1.8^{+0.9}_{-1.0}$ Myr after the formation of CAIs (Dauphas and Pourmand, 2011; Kobayashi and Dauphas, 2013). ^{60}Fe-^{60}Ni dating techniques provides a robust lower limit of $1.9\ ^{+17}_{-0.8}$ Myr after CAI formation in which the core of Mars reached ~44% of its present size (Tang & Dauphas, 2014). Iron meteorite parent bodies are modeled to have formed in < 0.5 Myr after CAI formation (Scott, 2006). With the aid of Mo and W

isotope measurements in iron meteorites, it is inferred that Jupiter's core grew to about 20 Earth mass less than 1 million years after CAI formation (Kruijer et al., 2017).

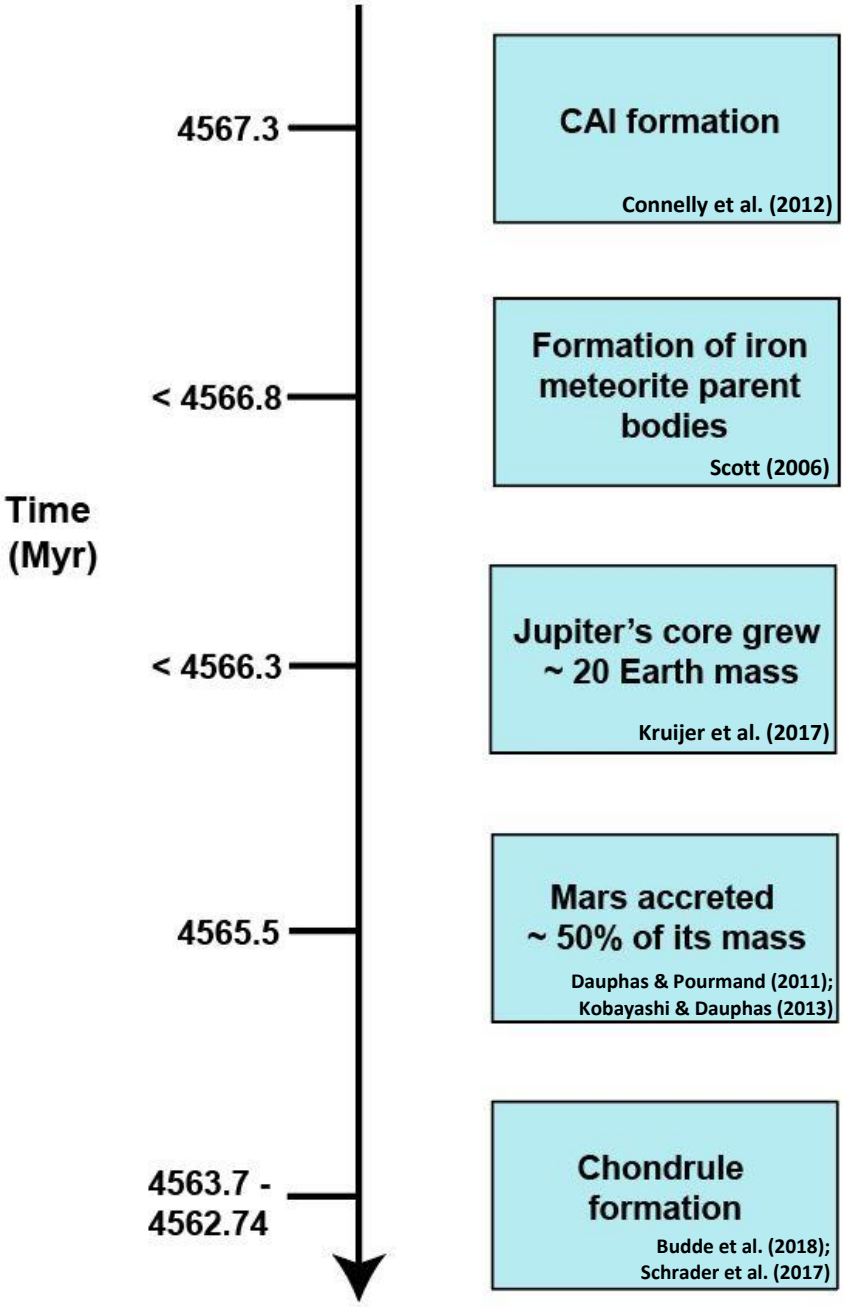

Figure 34. Timeline showing evidence that planet building was already underway between the formation of CAIs and chondrules.

CHAPTER 5

CONCLUSION

I have conducted a suite of dynamic crystallization experiments on chondrule analogs, with the compositions of FeO-poor chondrules, and considering both fine-grained and coarse-grained precursors. I melted and cooled these samples, systematically exploring 133 combinations of parameters, including precursor grain size, peak temperature, heating duration, and cooling rate through the crystallization temperature range. The goal is to identify those parameters that reproduce the most common chondrule textures: barred, radial, and especially porphyritic, which dominates the textures of natural chondrules. This work classified the textures of the chondrule analogs using BSE imaging, and compare these to natural chondrules. Results show that many of the chondrules have transitional textures between the traditionally defined categories. Traditional porphyritic textures are produced with cooling rates ≤ 600 K/hr, heating durations of 1 minute (but not 5 minutes), and using relatively coarse-grained precursors (> 200 μm). Production of porphyritic textures is less sensitive to peak temperature across the range we considered (50 K below to 50 K above the liquidus). It is noted that skeletal overgrowths are a common feature of porphyritic chondrules produced at these fast cooling rates, but that natural chondrules often show similar features, suggesting that while porphyritic textures can be reproduced at slower cooling rates, natural chondrules may be more consistent with cooling rates near 600 K/hr. Barred and radial textures are generally produced by complete dissolution of seed nuclei, caused by longer heating durations (≥ 5 minutes) and/or finer-grained (< 90 μm) precursors. Faster cooling rates ≥ 1000 K/hr are consistent with barred or radial textures, but not porphyritic.

This work identifies heating duration as a major determinant of chondrule textures, with otherwise identical conditions leading to porphyritic textures with 1 minute of peak heating, and non-porphyritic textures with 5 minutes of peak heating. Retention of volatiles like Na have previously constrained the duration of peak heating above the liquidus to < 10 minutes (Yu & Hewins 1998), but this work has also constrained this parameter by measuring the rate of chemical dissolution of relict grains, following the approach of Soulié et al. (2017). Retention of seed nuclei needed for porphyritic textures are constrained by chemical dissolution rates to require heating durations less than 10 minutes at most, consistent with the findings. This imposes tight constraints on models of chondrule formation. Unfortunately, a large number of dynamic crystallization experiments in the literature explored heating durations much longer than 10 minutes. Connolly et al. (1998) was the only one to explore production of porphyritic textures with short heating durations. The results presented here are in accord with theirs, that cooling rates of 500 – 600 K/hr are near the maximum cooling rate that can produce porphyritic textures, although this limit should be tested with smaller precursor grain sizes.

Planetary embryo bow shocks, especially adiabatic shocks with speeds ≈ 6 km/s, naturally predict peak temperatures near typical chondrule liquidus temperatures, short heating durations, and cooling rates near or exceeding 600 K/hr, assuming an embryo radius 3000 km), possibly as low as 450 K/hr, assuming an embryo radius 4000 km (Mann et al. 2016). The planetary embryo bow shock model therefore still remains a viable chondrule mechanism for the formation of the vast majority of chondrules. The results presented here therefore strongly suggest that large planetary embryos were present and on eccentric orbits during the first few million years of the Solar System's

history. A significant implication is that chondrules do not necessarily constitute the building blocks of planets. Rather, the chondrules in chondrites in our collections represent a byproduct of planet formation that had already largely taken place.

REFERENCES

Alexander, C. M., Grossman, J. N., Ebel, D. S., and Ciesla F. J. (2008). The formation conditions of chondrules and chondrites. *Science, 320*, 1617–1619.

Amelin, Y., and Krot, A. (2007). Pb isotopic age of the Allende chondrules. *Meteoritics and Planetary Science, 42*(7-8), 1321-1335.

Anders, E. (1964). Origin, age and composition of meteorites. *Space Sci. Rev*. 3, 583-714.

Arakawa, S., and Nakamoto, T. (2016). Compound chondrule formation via collision of supercooled droplets. *Icarus, 276*, 102-106.

Asphaug, E., Jutzi, M., and Movshovitz, N. (2011b). Chondrule formation during planetesimal accretion. *Earth and Planetary Science Letters, 308*(3), 369-379.

Berlin J., Jones R., and Brearley, A. (2011). Fe-Mn systematics of type IIA chondrules in unequilibrated CO, CR, and ordinary chondrites. *Meteoritics and Planetary Science*. *46*, 513-533.

Bland, P. A., Alard, O., Benedix, G. K., Kearsley, A. T., Menzies, O. N., Watt, L. E., and Rogers, N. W. (2005). Volatile fractionation in the early solar system and chondrule/matrix complementarity. *Proc. Natl. Acad. Sci*. USA 102, 13755–13760.

Boley, A., Morris, M., and Desch, S. J. (2013). High-Temperature Processing of Solids Through Solar Nebular Bow Shocks: 3d Radiation Hydrodynamics Simulations with Particles. *The Astrophysical Journal, 776*(2), 23.

Boss, A. P. (2002). Evolution of the solar nebula. V. Disk instabilities with varied thermodynamics. *The Astrophysical Journal, 576*,462–472.

Boss, A. P., and Durisen, R. (2005). Chondrule-forming Shock Fronts in the Solar Nebula: A Possible Unified Scenario for Planet and Chondrite Formation. *The Astrophysical Journal, 621*(2), L137-L140.

Budde, G., Kruijer, T. S., and Kleine, T. (2018). Hf-W chronology of CR chondrites: Implications for the timescales of chondrule formation and the distribution of ^{26}Al in the solar nebula. *Geochimica et Cosmochimica Acta, 222*, 284-304.

Campbell, A. J., Humayun, M., and Weisberg, M. K. (2002). Siderophile element constraints on the formation of metal in the metal-rich chondrites. *Geochimica et Cosmochimica Acta, 66*, 647–660.

Ciesla, F. J., Hood, L. L., and Weidenschilling, S. J. (2004a). Evaluating planetesimal bow shocks as sites for chondrule formation. *Meteoritics and Planetary Science, 39*,1809–1821.

Ciesla, F. J., Lauretta, D. S., and Hood, L. L. (2004). The frequency of compound chondrules and implications for chondrule formation. *Meteoritics and Planetary Science, 39*, 531–544.

Connolly, H. C. Jr. and Hewins, R. H. (1991). The influence of bulk composition and dynamic melting conditions on olivine chondrule textures. *Geochimica et Cosmochimica Acta, 55*, 2943–2950.

Connolly, H. C., Jr., Hewins, R. H., Ash, R. D., Zanda, B., Lofgren, G. E., and Bourot-Denise, M. (1994). Carbon and the formation of reduced chondrules. *Nature*, *371*, 136-139.

Connolly, H. C., Jones, B. D., and Hewins, R. H. (1998). The flash melting of chondrules: An experimental investigation into the melting history and physical nature of chondrule precursors. *Geochimica et Cosmochimica Acta*, *62*(15), 2725-2735.

Connelly, J., Bizzarro, M., Krot, A., Nordlund, A., Wielandt, D., and Ivanova, M. (2012). The absolute chronology and thermal processing of solids in the solar protoplanetary disk. *Science*, *338*(6107), 651-655.

Dauphas, N. and Pourmand, A. (2011). Hf–W–Th evidence for rapid growth of Mars and its status as a planetary embryo. *Nature*, *473*(7348), 489-492.

DeHart, J. M., and Lofgren, G. E. (1996). Experimental studies of group A1 chondrules. *Geochimica et Cosmochimica Acta, 60*, 2233–2242.

Desch, S. J. and Cuzzi, J. N. (2000). The generation of lightning in the solar nebula. *Icarus, 143*, 87–105.

Desch, S. J. and Turner, N. (2015). High-Temperature Ionization in Protoplanetary Disks. *The Astrophysical Journal*, *811*(2), 16.

Desch, S. J., Morris, M. A., Connolly, H. C., and Boss, A. P. (2010). A critical examination of the X-wind model for chondrule and calcium-rich, aluminum-rich inclusion formation and radionuclide production. *The Astrophysical Journal*, *725*, 692–711.

Desch, S. J., Morris, M. A., Connolly, H. C., and Boss, A. P. (2012). The importance of experiments: Constraints on chondrule formation models. *Meteoritics and Planetary Science, 47*(7), 1139-1156.

Dodd, R. (1981). Meteorites, a petrologic-chemical synthesis. Cambridge [Cambridgeshire]; New York: Cambridge University Press.

Donaldson, C. H. (1976). An experimental investigation of olivine morphology. *Contributions to Mineralogy and Petrology, 57*, 187-213.

Gooding, J. L., Keil, K., (1981). Relative abundances of chondrule primary textural types in ordinary chondrites and their bearing on conditions of chondrule formation. *Meteoritics, 16,* 17–43.

Grove, T. L. (1982). Use of Fe Pt alloys to eliminate the iron loss problem in 1 atmosphere gas mixing experiments: Theoretical and practical considerations. *Contributions to Mineralogy and Petrology*, *78*(3), 298-304.

Hammer, J. E. (2006). Influence of fO2 and cooling rate on the kinetics and energetics of Fe-rich basalt crystallization. *Earth Planet. Sci. Lett*., *248*, 618-637.

Herzberg, C. T. (1979). The solubility of olivine in basaltic liquids: An ionic model. *Geochimica et Cosmochimica Acta, 43*(8), 1241-1251.

Hewins, R. H., and Fox, G. E. (2004). Chondrule textures and precursor grain size: An experimental study. *Geochimica et Cosmochimica Acta, 68*(4), 917-926.

Hewins, R. H., Klein L. C., & Fasano, B.V. (1981). Conditions of formation of pyroxene excentroradial chondrules. *Proc. Lunar Planet. Sci., 12B*, 1123-1133.

Hood, L. L. (1998). Thermal processing of chondrule and CAI precursors in planetesimal bow shocks. *Meteoritics and Planetary Science, 33*, 97–107.

Hood, L. L., and Horanyi, M. (1991). Gas dynamic heating of chondrule precursor grains in the solar nebula. *Icarus, 93*, 259-269.

Hood, L. L., and Weidenschilling, S. (2012). The planetesimal bow shock model for chondrule formation: A more quantitative assessment of the standard (fixed Jupiter) case. *Meteoritics and Planetary Science, 47*(11), 1715-1727.

Johnson, B. C, Minton, D. A., Melosh, H. J., and Zuber, M. T. (2015). Impact jetting as the origin of chondrules. *Nature, 517*, 339-341.

Jones, R. H., Grossman, J. N., and Rubin, A. E. (2005). *ASP Conf. Ser. 341, Chemical, Mineralogical and Isotopic Properties of Chondrules: Clues to Their Origin ed A. N. Krot, E. R. D. Scott and B. Reipurth (San Francisco, CA: ASP) 251.*

Jones, R. H. (2012). Petrographic constraints on the diversity of chondrule reservoirs in the protoplanetary disk. *Meteoritics and Planetary Science, 47*(7), 1176-1190.

Jones, R. H. and Lofgren, G. E. (1993). A comparison of FeO-rich, porphyritic olivine chondrules in unequilibrated chondrites and experimental analogues. *Meteoritics, 28*, 213–221.

Joung, M., Mac Low, M., and Ebel, D. (2004). Chondrule Formation and Protoplanetary Disk Heating by Current Sheets in Nonideal Magnetohydrodynamic Turbulence. *The Astrophysical Journal*, *606*(1), 532-541.

Kennedy, A. K., Lofgren, G. E., and Wasserburg, G. J. (1993). An experimental study of trace element partitioning between olivine, orthopyroxene and melt in chondrules—Equilibrium values and kinetic effects. *Earth and Planetary Science Letters, 115*, 177–193.

Kita, N. T., and Ushikubo, T. (2012). Evolution of protoplanetary disk inferred from 26Al chronology of individual chondrules. *Meteoritics and Planetary Science, 47*(7), 1108-1119.

Kita, N. T., Nagahara, H., Togashi, S., and Morishita, Y. (2000). A short duration of chondrule formation in the solar nebula: Evidence from ^{26}Al in Semarkona ferromagnesian chondrules. *Geochimica et Cosmochimica Acta, 64*, 3913–3922.

Kobayashi, H. and Dauphas, N. (2013). Small planetesimals in a massive disk formed Mars. *Icarus*, *225*(1), 122-130.

Krot, A. N. and Nagashima, K. (2017). Constraints on mechanisms of chondrule formation from chondrule precursors and chronology of transient heating events in the protoplanetary disk. *Geochem. J. 51*, 45–68.

Krot, A. N., Nagashima, K., Van Kooten, E. M. M., and Bizzarro, M. (2017). High-temperature rims around calcium–aluminum-rich inclusions from the CR, CB and CH carbonaceous chondrites. *Geochimica et Cosmochimica Acta, 201*, 155-184.

Kruijer, T., Burkhardt, C., Budde, G., and Kleine, T. (2017). Age of Jupiter inferred from the distinct genetics and formation times of meteorites., *Proceedings of the National Academy of Sciences of the United States of America*, 6712-6716.

Leroux, H., Libourel, G., Lemelle, L., and Guyot, F. (2003). Experimental study and TEM characterization of dusty olivines in chondrites: Evidence for formation by in situ reduction. *Meteoritics and Planetary Science*, *38*(1), 81-94.

Lichtenberg, T., Golabek, G. J., Dullemond, C. P., Schönbächler, M., Gerya, T. V., & Meyer, M. R. (2018). Impact splash chondrule formation during planetesimal recycling. *Icarus. 302*, 27-43.

Lofgren, G. E. (1989). Limits on chondrule formation processes imposed by dynamic crystallization experiments. *Meteoritics, 24*, 294.

Lofgren, G. E. (1989). Dynamic crystallization of chondrule melts of porphyritic olivine compositon; textures experimental and natural. *Geochimica et Cosmochimica Acta, 53(2)*, 461-470.

Lofgren, G. E. and Lanier, A. B. (1990). Dynamic crystallization study of barred olivine chondrules. *Geochimica et Cosmochimica Acta, 54*, 3537–3551.

Lofgren, G. E., and Russell, W. J. (1986). Dynamic crystallization of chondrule melts of porphyritic and radial pyroxene composition. *Geochimica et Cosmochimica Acta, 50*(8), 1715-1726.

Mann, C., Boley, A. P., and Morris, M. (2016). Planetary Embryo Bow Shocks as A Mechanism for Chondrule Formation. *The Astrophysical Journal,818*(2), 20.

McNally, C. (2013). Mineral Processing by Short Circuits in Protoplanetary Disks. *Astrophysical Journal Letters*, 767(1), Astrophysical Journal Letters, 2013, Vol.767(1).

Morris, M., Weidenschilling, S J., Desch, S. J. (2016). The effect of multiple particle sizes on cooling rates of chondrules produced in large-scale shocks in the solar nebula. *Meteoritics and Planetary Science, 51*(5), 870-884.

Morris, M., Boley, A., Desch, S., and Athanassiadou, T. (2012). Chondrule formation in bow shocks around eccentric planetary embryo. *The Astrophysical Journal, 752*(1), 17.

Nettles, J., Lofgren, G., Carlson, W., and McSween, H. (2006). Extent of chondrule melting: Evaluation of experimental textures, nominal grain size, and convolution index. *Meteoritics and Planetary Science, 41*(7), 1059-1071.

Radomsky, P. M. and Hewins, R. H. (1990). Formation conditions of pyroxene-olivine and magnesian olivine chondrules. *Geochimica et Cosmochimica Acta, 54*, 3475–3490.

Scott, E. (2006). Meteoritical and dynamical constraints on the growth mechanisms and formation times of asteroids and Jupiter. *Icarus, 185*(1), 72-82.

Schrader, D. L., Nagashima, K., Krot, A. N., Ogliore, R. C., Yin, Q.-Z., Amelin, Y. A., Stirling, C. H., and Kaltenbach, A. (2017). Distribution of ^{26}Al in the CR chondrite chondrule-forming region of the protoplanetary disk. *Geochimica et Cosmochimica Acta, 201*, 275–302.

Schrader, D. L., Nagashima, K., Waitukaitis, S. R., Davidson, J., McCoy, T. J., Connolly, Jr. H. C., and Lauretta, D. S. (2018). The retention of dust in protoplanetary disks: Evidence from agglomeratic olivine chondrules from the outer Solar System. *Geochimica et Cosmochimica Acta, 223*, 405–421.

Shu, F. H., Shang, H., and Lee, T. (1996). Toward an astrophysical theory of chondrites. *Science, 271*,1545–1552.

Shu, F. H., Shang, H., Glassgold, A. E., and Lee, T. (1997). X-rays and fluctuating X-winds from protostars. *Science, 277*, 1475–1479.

Shu, F. H., Shang, H., Gounelle, M., Glassgold, A. E., and Lee, T. (2001). The origin of chondrules and refractory inclusions in chondritic meteorites. *The Astrophysical Journal, 548*, 1029–1050.

Soulié, C., Libourel, G., and Tissandier, L. (2017). Olivine dissolution in molten silicates: An experimental study with application to chondrule formation. *Meteoritics & Planetary Science, 52*(2), 225-250.

Tang, H. and Dauphas, N. (2014). 60Fe–60Ni chronology of core formation in Mars. *Earth and Planetary Science Letters, 390*, 264-274.5

Tsuchiyama, A., Osada, Y., Nakano, T., and Uesugi, K. (2004). Experimental reproduction of classic barred olivine chondrules: Open-system behavior of chondrule formation. *Geochimica et Cosmochimica Acta, 68*, 653–672.

Urey, H. C. and Craig, H. (1953). The composition of the stone meteorites and the origin of the meteorites. *Geochimica et Cosmochimica Acta, 4*, 36–82.

Villeneuve, J., Chaussidon, M., and Libourel, G. (2009). Homogeneous distribution of ^{26}Al in the solar system from the Mg isotopic composition of chondrules. *Science, 325*, 985-988.

Wick, M. J. and Jones, R. H. (2012). Formation conditions of plagioclase-bearing type I chondrules in CO chondrites: A study of natural samples and experimental analogs. *Geochimica et Cosmochimica Acta, 98,* 140–159.

Wasson, J. T. and Kallemeyn, G. W. (1990). Allan Hills 85085 – a subchondritic meteorite of mixed nebular and regolitic heritage. *Earth Planet. Sci. Lett. 101,* 3175–3183.

Wasson, J. T., Krot, A. N., Lee, M. S., and Rubin, A. E., (1995). Compound chondrules. *Geochimica et Cosmochimica Acta, 59,* 1847–1869.

Weisberg, M. K., McCoy, T. J., and Krot, A. N. (2006). Systematics and evaluation of meteorite classification. In: D.S. Lauretta and H.Y. McSween Jr. (eds.), *Meteorites and the Early Solar System II*, University of Arizona Press, Tuscon, 19-52.

Wood J. A. (1996). Processing of chondritic and planetary material in spiral density waves in the nebula. *Meteoritics and Planetary Science*, *31*, 641–645.

Young, E. D., Tonui, E., Manning, C. E., Schauble, E., and Macris, C. A. (2009). Spinel–olivine magnesium isotope thermometry in the mantle and implications for the mg isotopic composition of earth. *Earth and Planetary Science Letters, 288*(3), 524-533.

Yu, Y., and Hewins, R. H. (1997). Transient heating and chondrule formation: evidence from sodium loss in flash heating simulation experiments. *Geochimica et Cosmochimica Acta,* 62,159-172

APPENDIX A

SUMMARY OF EXPERIMENTAL RUNS

Table A1. Summary of experimental runs.

Sample	Grain Size	Peak Temperature (°C)	Heating Duration (mins)	Cooling Rate (K/hr)	Texture
61	n.a.	1400	1	1000	euhedral to subhedral grain fragments
62	n.a.	1400	1	1000	euhedral to subhedral grain fragments
63	n.a.	1400	1	1000	euhedral to subhedral grain fragments
69	n.a.	1400	1	3000	euhedral to subhedral grain fragments
70	n.a.	1400	1	3000	euhedral to subhedral grain fragments
71	FL	1400	1	3000	large euhedral grain
74	FL	1400	10	1000	euhedral to subhedral grain fragments
77	FL	1400	10	1000	euhedral to subhedral grain fragments
78	FL	1400	20	1000	euhedral to subhedral grain fragments
79	FL	1400	20	1000	euhedral to subhedral grain fragments
80	FL	1400	15	1000	euhedral to subhedral grain fragments
82	FL	1400	10	1000	euhedral to subhedral grain fragments
83	FL	1400	10	1000	euhedral to subhedral grain fragments
85	FL	1400	1	1000	euhedral to subhedral grain fragments
87	FL	1400	10	1000	large subhedral grain
91	FL	1400	5	1000	euhedral to subhedral grain fragments

92	FL	1400	10	1000	euhedral to subhedral grain fragments
95	FL	1608	10	1000	glass
96	FL	1608	5	1000	subhedral grains, relict cores, skeletal rim growth, plate, hopper, feather
97	FL	1608	1	1000	single large anhedral grain, relict core, skeletal growth, plate, feather
98	FL	1558	1	1000	anhedral to subhedral grains, skeletal rim growth, plate, feather
103	FL	1608	10	instant	glass
104	FL	1608	10	5000	glass
105	FL	1608	10	1000	euhedral to subhedral grains, relict cores, skeletal rim growth, hopper, porphyritic-like texture
106	FL	1608	10	5000	spinifex, chain, plate, barred-like texture
107	FL	1608	5	5000	subhedral grains, relict cores, skeletal rim growth, hopper, feather
108	FL	1608	1	5000	euhedral to subhedral grains, relict cores, skeletal rim growth, hopper, feather
109	FL	1608	10	5000	spinifex, chain, plate, barred-like texture
110	FL	1608	10	5000	euhedral to subhedral grains, relict cores, skeletal rim growth, hopper
111	FL	1658	10	5000	subhedral grains, relict cores, skeletal rim growth, spinifex, chain, hopper
112	FL	1558	10	5000	glass
113	FL	1608	10	3000	glass

114	FF	1608	10	5000	glass
115	FF	1608	10	instant	spinifex, chain, plate
119	FL	1558	10	5000	spinifex, chain, plate, barred-like texture
121	FF	1558	5	5000	spinifex, chain, plate
122	FF	1558	10	5000	spinifex, chain, plate, barred/radial-like texture
123	FL	1558	1	5000	spinifex, chain, plate
124	FL	1558	5	5000	spinifex, chain, plate
125	FF	1558	1	5000	feather
126	FF	1608	1	5000	spinifex, chain, plate
127	FF	1608	5	5000	spinifex, chain
129	FL	1608	5	1000	spinifex, chain, plate, barred-like texture
131	FL	1608	10	1000	spinifex, chain, plate, barred-like texture
132	FL	1608	10	3000	spinifex, chain, dendritic
133	FF	1608	10	1000	spinifex, chain, plate, barred-like texture
138	FL	1608	10	5000	subhedral grains, relict cores, skeletal rim growth, spinifex, chain
139	FL	1608	5	5000	subhedral grains, relict cores, skeletal rim growth, spinifex, chain
140	FL	1608	1	5000	subhedral grains, relict cores, skeletal rim growth, spinifex, chain
141	FL	1608	15	5000	anhedral grains, relict cores, skeletal rim growth, spinifex, hopper, feather
142	FL	1608	10	1000	subhedral grains, relict cores, skeletal rim growth
143	FL	1658	10	5000	glass

144	FF	1558	10	1000	euhedral to subhedral grains, relict cores, hopper
145	FF	1658	10	3000	glass
147	FL	1658	10	5000	euhedral to subhedral grains, relict cores, skeletal rim growth, hopper
148	FF	1608	10	3000	spinifex, chain
149	FL	1608	10	3000	euhedral grains, relict cores, skeletal rim growth, feather
150	FL	1558	10	3000	euhedral grains, hopper, porphyritic-like texture
151	FF	1558	1	3000	euhedral to subhedral grains, relict cores, skeletal rim growth
152	FL	1658	1	3000	euhedral to subhedral grains, relict cores, skeletal rim growth, hopper
153	FL	1608	5	3000	euhedral to subhedral grains, relict cores, skeletal rim growth, spinifex, hopper
154	FL	1608	1	3000	euhedral to subhedral grains, relict cores, skeletal rim growth, hopper
155	FL	1558	5	3000	euhedral to subhedral grains, relict cores, skeletal rim growth
156	FL	1558	10	1000	subhedral grains, relict cores, skeletal rim growth, hopper, porphyritic-like texture
160	FF	1558	1	1000	euhedral to subhedral grains, relict cores, chain, hopper
161	FF	1658	1	5000	spinifex, chain, plate, dendritic
162	FF	1658	5	5000	glass
163	FF	1658	10	5000	glass
164	FL	1658	1	5000	glass

165	FL	1658	5	5000	spinifex, chain, plate, barred-like texture
166	FL	1658	10	1000	glass
167	FF	1558	5	3000	euhedral to subhedral grains, relict cores, hopper
168	FL	1658	10	3000	glass
169	FF	1558	5	1000	euhedral grains, relict cores, spinifex, chain, hopper
170	FL	1558	5	1000	euhedral to subhedral grains, relict cores, spinifex, chain, hopper
171	FF	1608	1	1000	euhedral grains, relict cores, hopper
172	FF	1608	5	1000	spinifex, chain, plate, barred-like texture
173	FL	1608	1	1000	euhedral to subhedral grains, relict cores, skeletal rim growth, chain, hopper
174	FF	1658	1	1000	radial-like texture
175	FF	1658	5	1000	spinifex, chain, plate, dendritic, barred-like texture
176	FF	1658	5	3000	spinifex, hopper
177	FL	1658	1	1000	euhedral to subhedral grains, relict cores, skeletal rim growth, hopper
178	FL	1558	1	3000	spinifex, hopper
179	FL	1658	5	3000	radial-like texture
180	FF	1658	10	1000	glass
181	FF	1658	1	3000	glass
182	FF	1608	5	3000	spinifex, chain, plate, barred-like texture
183	FF	1608	1	3000	spinifex, dendritic
188	FL	1658	10	600	chain, hopper
189	FF	1658	10	600	euhedral grains, hopper

190	FL	1608	10	600	chain, hopper
191	FF	1608	10	600	glass
192	FL	1558	1	600	euhedral to subhedral grains, relict cores, hopper
193	FF	1558	10	600	euhedral grains, hopper
194	FL	1558	10	600	euhedral grains, relict cores, hopper
195	FL	1658	5	600	spinifex, chain, plate, barred-like texture
196	FF	1658	5	600	spinifex, chain, plate, barred-like texture
197	FL	1608	5	600	glass
198	FL	1658	1	600	euhedral to subhedral grains, relict cores, skeletal rim growth, hopper, porphyritic-like texture
199	FF	1658	5	600	spinifex, chain, plate, barred-like texture
200	FF	1658	1	600	euhedral to subhedral grains, relict cores, skeletal rim growth, hopper, porphyritic-like texture
201	FF	1658	1	600	euhedral grains, chain, hopper
202	FF	1608	1	600	glass
204	FF	1608	1	600	euhedral grains, chain, hopper
205	FL	1558	5	600	euhedral to subhedral grains, relict cores, skeletal rim growth, porphyritic-like texture
206	FF	1558	5	600	euhedral to subhedral grains, relict cores, hopper
207	FF	1608	10	300	hopper, lattice
208	FF	1608	1	300	single large euhedral grain, hopper

209	FF	1608	5	300	spinifex, chain, plate, barred-like texture
210	FF	1608	10	300	spinifex, chain, hopper
211	FF	1658	1	300	spinifex, chain, plate, barred-like texture
212	FF	1558	10	300	euhedral grains, hopper
214	FL	1558	1	300	euhedral to subhedral grains, relict cores, skeletal rim growth, porphyritic-like texture
215	FL	1608	10	300	euhedral grains, hopper
216	FL	1658	10	300	spinifex, chain, plate, barred-like texture
217	FF	1658	10	300	spinifex, chain, plate, barred-like texture
218	FF	1558	1	300	euhedral to subhedral grains, relict cores, hopper
219	FL	1608	5	300	euhedral to subhedral grains, relict cores, skeletal rim growth, porphyritic-like texture
220	FF	1658	5	300	spinifex, chain, plate, dendritic, barred-like texture
221	FL	1658	1	300	radial-like texture
222	FL	1608	1	300	euhedral to subhedral grains, hopper
223	FL	1558	10	300	euhedral to subhedral grains, relict cores, hopper
224	FF	1558	5	300	euhedral to subhedral grains, relict cores, hopper

FF: albite + diopside + olivine (63 – 90 μm)
FL: albite (63 – 90 μm) + diopside (63 – 90 μm) + olivine (212 – 250 μm)